

15 **Abstract**

16 Stratiform and convective precipitation are known to be associated with distinct isotopic
17 fingerprints in the tropics. Such rain type specific isotope signals are of key importance for
18 climate proxies based on stable isotopes like for example ice cores and tree rings and can be used
19 for climate reconstructions of convective activity. However, recently, the relation between rain
20 type and isotope signal has been intensively discussed. While some studies point out the
21 importance of deep convection for strongly depleted isotope signals in precipitation, other
22 studies emphasize the role of stratiform precipitation for low concentrations of the heavy water
23 isotopes. Uncertainties arise from observational studies as they mainly consider oceanic regions
24 and mostly long aggregation timescales, while modelling approaches with global climate models
25 cannot explicitly resolve convective processes and rely on parametrization. As high-resolution
26 climate models are particularly important for studies over complex topography, we applied the
27 isotope-enabled version of the high-resolution climate model from the Consortium for Small-
28 Scale Modelling (COSMO_{iso}) over the Andes of tropical south Ecuador, South America, to
29 investigate the influence of stratiform and convective rain on the stable oxygen isotope signal of
30 precipitation ($\delta^{18}\text{O}_p$). Our results highlight the importance of deep convection for depleting the
31 isotopic signal of precipitation and increasing the secondary isotope variable deuterium excess.
32 Moreover, we found that an opposing effect of shallow and deep convection on the $\delta^{18}\text{O}_p$ signal.
33 Based on these results, we introduce a shallow and deep convective fraction to analyze the effect
34 of rain types on $\delta^{18}\text{O}_p$.

35 **Plain Language Summary**

36 Tropical rainfall can be classified as convective and stratiform rain, which carry fingerprints in
37 their water isotope signal. This implies that climate reconstructions of convective activity can be
38 made, because the isotopic signal in precipitation is conserved in climate archives like ice cores
39 or tree rings. Contrasting results emerged from observations, due to data scarcity, and from
40 global climate models, which have shortcomings due to coarse spatial and temporal resolutions.
41 We addressed the question of the influence of different rain types on the isotopic signal of
42 precipitation by using a high-resolution, isotope-enabled climate model over the tropical Andes.
43 We found out that particularly deep convection leads to the most negative values, whereas
44 stratiform rain and shallow convection are related to less negative, even slightly positive isotope
45 values. Consequently, it is unavoidable to consider the subclasses shallow and deep convection
46 separately, which is why we suggest a shallow and deep convective fraction for analyzing the
47 effect of rain types on the isotopic signal.

48 **Keywords**

49 Stable Water Isotopes – Precipitation – High-Resolution, Isotope-Enabled Climate Modeling –
50 Tropical South America – Ecuador – Convection

51 **1 Introduction**

52 The stable isotopes of oxygen and hydrogen can be used to reconstruct past changes in
53 the hydrological cycle based on the isotopic signals conserved in climate archives like ice cores,
54 lake or ocean sediments and tree rings (Dee et al., 2023; Gat, 1996; Hoffmann et al., 2003;
55 McCarroll & Loader, 2004; Thompson et al., 2000). To improve the reliability of such
56 reconstructions a thorough understanding of the atmospheric processes influencing the isotopic
57 composition of precipitation is necessary.

58 The stable oxygen and hydrogen isotope ratio of precipitation ($\delta^{18}\text{O}_P$ and δD_P ,
59 respectively) is defined as the ratio of the heavier (^{18}O , ^2H or D) to the lighter isotope (^{16}O , ^1H)
60 with respect to standard mean ocean water or to the Vienna Standard Mean Ocean Water
61 (VSMOW). The lower saturation vapor pressure and the heavier mass of the rare water
62 molecules (so called isotopologues) result in a preferential accumulation of lighter isotopes in
63 water vapor whereas the heavier isotopes tend to stay in the liquid phase. In the atmosphere, this
64 separation, called fractionation, occurs during phase changes and is related to equilibrium (e.g.
65 condensation) and kinetic or non-equilibrium (e.g. evaporation or deposition of vapor on ice
66 crystal) fractionation (Ciais & Jouzel, 1994; Dansgaard, 1964).

67 Deuterium excess (d-excess) in precipitation describes the linear relationship between
68 $\delta^{18}\text{O}_P$ and δD_P ($\text{d-excess} = \delta\text{D}_P - 8 * \delta^{18}\text{O}_P$) and is an indicator of non-equilibrium fractionation
69 (Dansgaard, 1964). It reflects the atmospheric conditions (relative humidity, sea surface
70 temperature) at the moisture sources of precipitation (Fröhlich et al., 2002; Merlivat & Jouzel,
71 1979; Pfahl & Sodemann, 2014), in-cloud ice formation processes (Ciais & Jouzel, 1994) or can
72 serve as an indicator of continental moisture recycling e.g., sub-cloud evaporation of raindrops
73 (Aemisegger et al., 2015; Graf et al., 2019) or evapotranspiration (Aemisegger et al., 2014;
74 Ampuero et al., 2020; Fröhlich et al., 2002).

75 In the tropics and particularly in marine environments, the so called 'amount effect' is
76 observed, i.e. increasing rain amounts are related to precipitation with low $\delta^{18}\text{O}_P$ values
77 (Dansgaard, 1964). However, the mechanisms behind the amount effect are complex and not
78 fully understood. It can partly be explained by the preferential removal of heavy isotopes from
79 the in-cloud water vapor during condensation. The remaining lighter water vapor forms the basis
80 for the following condensate and leads to a subsequent depletion of precipitation (Gat, 1996).
81 This is intensified by recycling effects in downdraft, i.e. evaporation of the falling rain and
82 diffusive exchanges with the ambient water vapor lead to a further depletion of the water vapor,
83 which is injected into the sub-cloud layer feeding the convective system (Risi et al., 2008).

84 Precipitation formation pathways can be classified into convective and stratiform.
85 Stratiform precipitation is typically associated with low rain rates and small upward velocities or
86 descending air below the cloud base. Convection, in contrast, features strong updrafts and high
87 rain rates (Houze, 2014; Mölders & Kramm, 2014). In the tropics, convection often co-occurs
88 with stratiform rain in so called mesoscale convective systems (MCSs) (Houze, 2004). These
89 have extents on the order of 100 km and are responsible for a large proportion of annual rainfall
90 in the tropics (Feng et al., 2021; Prein et al., 2022). The stratiform area of MCSs is fed by mid-
91 level inflow layers from the convective area. The melting at the 0°C atmospheric thermocline
92 (atmospheric melting layer) leads to cooling and hence to descending motions below the melting
93 layer. Slightly ascending air is usually recognized above the melting layer (Houze, 2014).

94 In recent studies, the depleting effect of different rain types on stable isotopes of water
95 vapor and precipitation has been intensely discussed (Aggarwal et al., 2016; Kurita, 2013; Kurita
96 et al., 2011; Lekshmy et al., 2014; Munksgaard et al., 2019; Tharammal et al., 2017). An
97 observational study in southern India found a relationship between the depleted $\delta^{18}\text{O}_P$ of
98 collected precipitation and the activity of MCSs (Lekshmy et al., 2014). Other studies pointed
99 out that particularly the stratiform precipitation within these MCSs is associated with a depleted
100 $\delta^{18}\text{O}_P$ signal, which was confirmed by a conceptual model (Kurita, 2013; Kurita et al., 2011) and,
101 in addition, by a significant negative correlation between measured monthly $\delta^{18}\text{O}_P$ and the
102 stratiform fraction of precipitation (Aggarwal et al., 2016). This relationship could also be shown

103 on a daily basis, however, some stations surprisingly revealed a positive correlation (Munksgaard
104 et al., 2019). These contrasting correlation signs were also present in modeling studies with
105 isotope-enabled general circulation models (GCMs) (Hu et al., 2018; Tharammal et al., 2017).
106 Uncertainty arises due to the unavoidable parameterization of convection and thus simplified
107 microphysical representation of convective rain formation in GCMs owing to their coarse spatial
108 and temporal resolutions, which is why these models cannot fully reproduce the impact of the
109 variability of convective systems (Houze et al., 2015) on precipitation isotope variability. To our
110 knowledge, no study has yet used isotope-enabled high-resolution regional climate models in this
111 respect, although these models can explicitly resolve convective processes - a tremendous
112 advantage in research questions on different precipitation types.

113 Previous studies of the relation between the isotope signature and precipitation type in the
114 tropics often focus on sites or model setups that are mainly considering maritime conditions
115 (Kurita, 2013; Kurita et al., 2011; Munksgaard et al., 2019; Risi et al., 2020). Although climate
116 proxies like tree rings or ice cores are located over land or in regions of complex topography,
117 studies in those areas are still scarce. In this respect, the tropical Andes are of particular interest
118 due to the contrasting air masses that approach the eastern and western flanks from the Atlantic
119 and Pacific, respectively (Landshuter et al., 2020; Trachte, 2018). These different background
120 states initiate different atmospheric processes, which are responsible for the formation of
121 precipitation and in turn influence its $\delta^{18}\text{O}_p$ signal.

122 The goal of this study is to analyze the influence of stratiform and convective
123 precipitation on the $\delta^{18}\text{O}_p$ of the eastern and western flanks of the Ecuadorian Andes. We use an
124 isotope-enabled and high-resolution climate model in a real-case setup, which is highly
125 advantageous for areas of complex topography and is needed to explicitly and realistically
126 simulate convective processes.

127 **2 Materials and Methods**

128 2.1 Description of Study Site

129 The study site in southern Ecuador is determined by the complex topography of the
130 meridionally orientated Andes (Figure 1) that act as a „climate divide“ (Emck, 2008). The
131 western flanks and the western lowlands of Ecuador are affected by the Pacific and exhibit one
132 clearly distinct rainy season from January to April (Garcia et al., 1998; Pucha-Cofrep et al.,
133 2015; Volland-Voigt et al., 2011). In contrast, the Andes in this region, show a bimodal
134 precipitation pattern with maxima in March to April and October to November (Garcia et al.,
135 1998). The Amazon is located east of the climate divide and is influenced by air masses from the
136 Atlantic. Precipitation in the Amazon falls during all months of the year with slightly higher
137 amounts during March and April (Garcia et al., 1998).

138 The seasonal variation of the so-called Intertropical Convergence Zone (ITCZ) is an
139 important feature determining the precipitation amounts in Ecuador. It propagates southward
140 around November, reaches its most southern position in January and passes Ecuador again
141 during its northward displacement from January to May. Stable isotope analysis of precipitation
142 in Ecuador pointed out that the passage of the ITCZ is, besides topographic forcing from the
143 Andes, a major mechanism for depleting heavy isotopes in precipitation (Garcia et al., 1998). In
144 addition, the El Niño Southern Oscillation (ENSO) phenomenon is responsible for the high inter-
145 annual variability of precipitation (Capotondi et al., 2015; McPhaden et al., 2006).

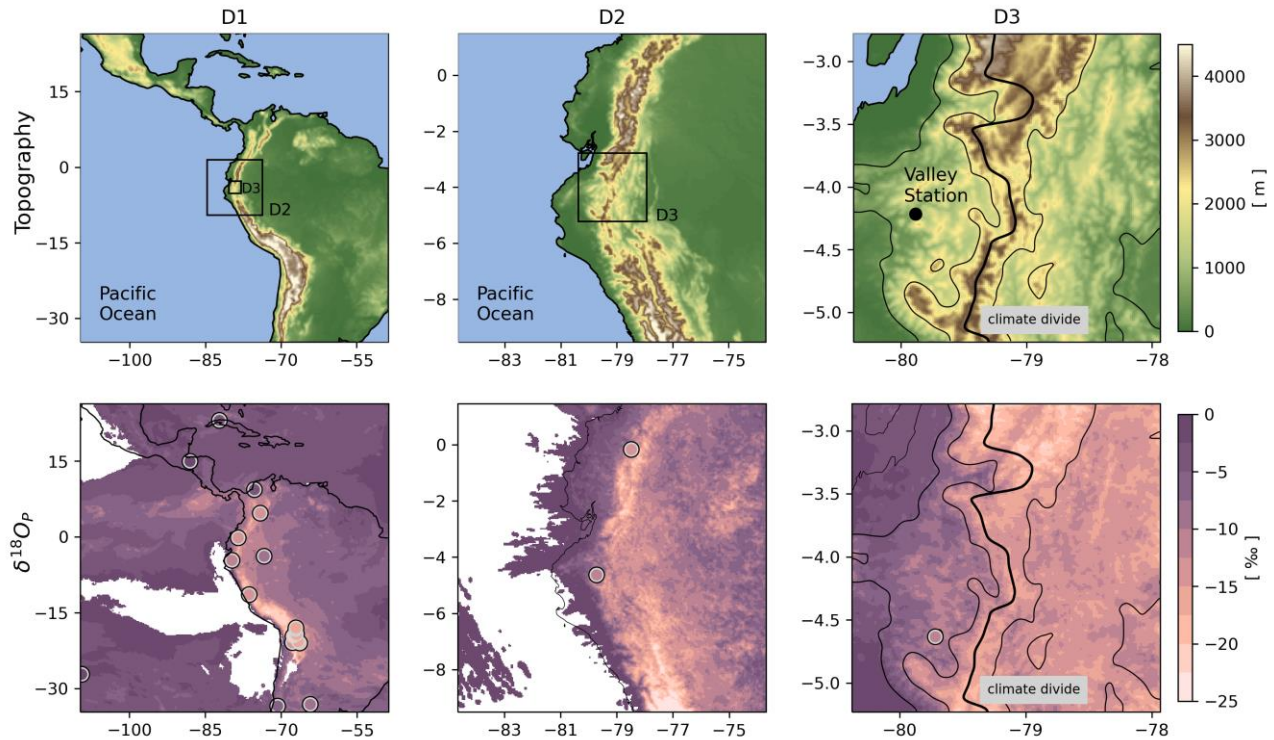


Figure 1. Topography of the study region and domain setup of the isotope-enabled version of the high-resolution climate model from the Consortium for Small-Scale Modelling (COSMO_{iso}) (first row). Seasonal rain rate weighted mean $\delta^{18}\text{O}_p$ of COSMO_{iso} evaluated against seasonal mean observations of the Global Network of Isotopes in Precipitation (GNIP) for the same period (January 2012 to April 2012, framed circles with color representing the $\delta^{18}\text{O}_p$ of the respective station) (second row). No data is available for white areas, which can be attributed to no precipitation. Although the second row shows results that are only discussed in Section 3, we include these maps here due to the topography dependency of these results.

146 This study is part of a project that tries to better understand the stable isotope signal in
 147 tree rings from the western flanks of the Andes in southern Ecuador (Landshuter et al., 2020).
 148 The availability of proxy data and observations at the same location is the reason for selecting
 149 this study site. However, the focus of this study is on the stable isotopes in precipitation, whereas
 150 the link to the stable isotopes of the tree rings is part of a follow-up study. We subdivided the
 151 area into four regions (Figure S1 in Supporting Information S1):

- 152 • Western Lowlands: below 500 m and west of the climate divide
- 153 • Western Flanks: above 500 m and below 2000 m and west of the climate divide
- 154 • Andes: above 2000 m
- 155 • Amazon: below 2000 m and east of the climate divide.

156 We limited the analyzed time period to the rainy season from January to April of 2012
 157 due to the computational costs and our focus on process understanding, which can be studied
 158 more efficiently in case-study frameworks than from very long records (e.g., Mölg et al., 2012).
 159 The examined months show enhanced precipitation amounts compared to the rest of the year in
 160 all defined regions. We chose the year 2012 as it was a year with moderate to high, but not

161 exceptionally high precipitation anomalies (Landshuter et al., 2020) that are linked to
162 anomalously warm sea surface temperatures in the eastern Pacific (Su et al., 2014).

163 2.2 Observations

164 2.2.1 Automatic Weather Station Data

165 Automatic Weather Stations (AWS) data was used from a deployment during a field
166 campaign from April 2007 to March 2015. The AWS were located in „Laipuna Valley“ (590 m
167 above sea level, -4.215°S, 79.885°W, Valley Station) and on „Laipuna Mountain“ (1,450 m
168 above sea level, -4.238°N, 79.899°W, Mountain Station) and recorded air temperature (at 2 m),
169 relative humidity (at 2 m), incoming short wave radiation (at 2 m), wind speed and direction (at
170 2 m) and precipitation (at 1 m) above the ground at 10-min intervals that were stored as hourly
171 means (Landshuter et al., 2020; Pucha-Cofrep et al., 2015; Spannll et al., 2016; Volland-Voigt et
172 al., 2011). To eliminate the temperature dependence of relative humidity, we also calculated and
173 used the water vapor pressure (Marshall & Plumb, 2008; Mölders & Kramm, 2014). Particularly,
174 the Valley Station was used to find a suitable model setup and to evaluate atmospheric variables
175 of the model output. The Mountain Station served as a reference for the variability that can be
176 expected nearby.

177 2.2.2 Satellite Retrievals

178 The MODERate resolution Imaging Spectroradiometer (MODIS) precipitable water
179 product is based on retrievals from the TERRA and AQUA satellites. The Level 2 dataset, which
180 reflects the column water-vapor amounts at 1 km spatial resolution during the day, is based on a
181 near-infrared algorithm (Gao, 2015). We used all available images from January 2012 to April
182 2012 of this satellite product to calculate its time mean for an independent spatial evaluation of
183 the modeled hydroclimate. The TERRA satellite passes the study region between 10:00 and
184 12:00 local time, whereas the AQUA satellite collects data between 13:00 and 15:00 local time.
185 In total 201 images were used covering the period from January 2012 to April 2012.

186 2.2.3 Stable Isotope Data From Precipitation

187 Monthly $\delta^{18}\text{O}_\text{P}$ data were downloaded from the Global Network of Isotopes in
188 precipitation (GNIP) database (IAEA/WMO, 2023). We selected all stations located in the study
189 area that provided at least three of the four monthly $\delta^{18}\text{O}_\text{P}$ values (from January to April 2012),
190 which resulted in twelve stations, for evaluating the $\delta^{18}\text{O}_\text{P}$ output of the isotope-enabled regional
191 climate model.

192 2.3 Isotope-Enabled High-Resolution Climate Model

193 The non-hydrostatic, limited-area numerical weather and climate model from the
194 Consortium for Small-Scale Modelling (COSMO) is based on an Arakawa C-grid on a rotated
195 geographical coordinate system in the horizontal and can be used with terrain-following Gal-
196 Chen height coordinates that flatten towards the top of the model domain (Steppeler et al., 2003).
197 Numerically the model is integrated with a third order Runge-Kutta scheme with the total
198 variation diminishing variant (Liu et al., 1994).

199 Its isotope-enabled version COSMO_{iso} (Pfahl et al., 2012) that we used in our study,
200 encompasses two additional parallel water cycles for each of the heavy isotopes (H_2^{18}O , HDO).

201 These water cycles do not affect other model components and can be interpreted as an individual
 202 copy of the usual water cycle of the light water molecule (H_2O) apart from fractionation
 203 processes during phase changes. No fractionation occurs in COSMO_{iso} during plant transpiration
 204 (Aemisegger et al., 2015). Fractionation processes during soil evaporation are account for by
 205 TERRAiso, an isotope-enabled prognostic multilayer soil model that is coupled to COSMO_{iso}
 206 (Christner et al., 2018). COSMO_{iso} has previously been used in numerous different studies
 207 (Aemisegger et al., 2015; Breil et al., 2020; Christner et al., 2018; Lee et al., 2019; Pfahl et al.,
 208 2012; Thurnherr et al., 2021) including tropical and subtropical regions (de Vries et al., 2022;
 209 Villiger et al., 2023).

210 In our study, we employed COSMO_{iso} for the first time over the complex topography of
 211 the Andes in tropical Ecuador, South America. We used a one-way nesting with a parent-to-child
 212 grid ratio of about three or five resulting in three domains of 22.5 km ($\sim 0.2025^\circ$, 330x330 grid
 213 cells), 4.5 km ($\sim 0.0405^\circ$, 300x300 grid cells) and 1.5 km ($\sim 0.0135^\circ$, 210x210 grid cells) grid
 214 spacing centered over southern Ecuador ($-4.0000^\circ N$, $79.1500^\circ W$); these domains are hereafter
 215 referred to as D1, D2 and D3, respectively (Figure 1). The model runs were performed with 50
 216 levels in the vertical from 1 January 2012, 06:00:00 local time until 30 April 2012 18:00:00 local
 217 time and stored with an hourly temporal resolution. The spin-up time of 48 hours was discarded
 218 for further analysis, which is why the analysis time interval starts on the 3 January 2012,
 219 06:00:00 local time. The increasing resolution from D1 to D3 requires modifications in the setup.
 220 We thus adjusted the time step, turbulent length, orography data and the width of the relaxation
 221 layer for each domain (Table 1).

222 *Table 1. COSMO_{iso} setup for resolution-dependent parameters with orography from the Global Land One-km Base
 223 Elevation Project (GLOBE) and the Advanced Spaceborne Thermal Emission and Reflection Radiometer (ASTER).*

Domain	Resolution	Number of Grid Cells (lon x lat)	Time Step (dt)	Turbulent length (tur_len)	Relaxation Layer (rlwidth)	Orography
D1	22.5 km ($\sim 0.2025^\circ$)	330x330	120 s	430 m	225 000 m	GLOBE (NOAA/NGDC)
D2	4.5 km ($\sim 0.0405^\circ$)	300x300	20 s	180 m	45 000 m	ASTER (METI/NASA)
D3	1.5 km ($\sim 0.0135^\circ$)	210x210	9 s	130 m	15 000 m	ASTER (METI/NASA)

224 The time steps are chosen to maintain the Courant number and are approximately linearly
 225 interpolated based on the spatial resolution thereby fulfilling the storage interval (3600 s) being a
 226 multiple of the time step (e.g. 120 s for D1). The asymptotic turbulent length (tur_len) is reduced
 227 to account for increasing turbulent fluxes with increasing resolution. This modification leads to
 228 steeper vertical gradients and enhanced instability in the boundary layer, which favors the
 229 initiation of convective processes (Baldauf et al., 2011). We followed the linear distribution as
 230 suggested by Vergara-Temprado et al. (2020).

231 Orographic features are highly dependent on the resolution, which is why we chose the
 232 orography from the Global Land One-km Base Elevation Project (GLOBE) for D1 and the finer
 233 resolved Advanced Spaceborne Thermal Emission and Reflection Radiometer (ASTER)
 234 orography for D2 and D3. Both were provided by the External Parameters for Numerical
 235 Weather Prediction and Climate Application (EXTPAR) (Asensio et al., 2020).

236 Lateral boundary information is transferred via the boundary zone (four grid cells at each
237 boundary of the subdomain) and the relaxation layer. The width of the relaxation layer (rlwidth)
238 should be 10 to 15 times the grid cell resolution in meters (Schättler et al., 2013). In our setup,
239 we applied this requirement and used the ten times the grid cell resolution requirement for all
240 domains. The grid cells of the boundary and relaxation layer are discarded for the data analysis.

241 The physical parameterization schemes that we used in our study are as follows: heating
242 rates by radiation are calculated once per hour by the scheme of Ritter and Geleyn (1992);
243 vertical turbulent diffusion is based on a 1-D prognostic equation for turbulent kinetic energy
244 (Mellor & Yamada, 1974); and microphysics of cloud and precipitation are represented with the
245 one-moment cloud ice scheme, which considers water vapor, cloud water as well as ice, rain and
246 snow (graupel and hail are not taken into account) (Doms et al., 2011). Regarding the
247 parameterization of convection for different spatial resolutions, there are different approaches
248 used and debated in the literature. While some argue that 7 km resolution or even less require a
249 parameterization (Fosser et al., 2015), others suggest that the explicit calculation or only
250 parameterized shallow convection is advantageous up to 25 km resolution (Vergara-Temprado et
251 al., 2020). After thoroughly testing different convection setups in terms of resolution, the
252 following one revealed the most realistic performance. In D1, we parameterized convection
253 using the Tiedtke (1989) scheme due to its coarse resolution. For D2 and D3, an explicit
254 treatment of convection yielded the most realistic accumulated precipitation amounts and
255 precipitation rates. The stable isotopes are only incorporated in the Tiedtke (1989) scheme,
256 which is why other parameterization schemes such as only for shallow convection could not be
257 applied.

258 Spectral nudging was conducted for zonal and meridional winds above 850 hPa only for
259 D1 to constrain drift in the large-scale circulation but allowing a freely evolving atmosphere in
260 D2 and D3. The height of the damping layer was adjusted to 18000 m (instead of 11000 m) as
261 proposed for a tropical setup of COSMO (Panitz et al., 2014). At this height the damping is zero
262 and increasing along a cosine damping profile to its maximum at the top of the model domain
263 (Schättler et al., 2013).

264 The atmospheric and stable isotope initial and boundary data were taken from ECHAM6-
265 wiso with temperature, vorticity, divergence and surface pressure fields nudged towards ERA5
266 (Cauquoin & Werner, 2021). The dataset has a spectral resolution of T127L95 (corresponding to
267 approx. $0.9^\circ \times 0.9^\circ$ horizontal resolution and 95 vertical levels) and a 6-hourly temporal
268 resolution. In this study and for all analyses, we calculated the rain rate weighted mean of $\delta^{18}\text{O}_p$
269 to be consistent with $\delta^{18}\text{O}_p$ of collected rain samples (Breil et al., 2020; IAEA/WMO, 2023).

270 The model runs were performed on the Fritz compute cluster at the Erlangen National
271 High Performance Computing Center (NHR@FAU) and was compiled with Intel 17.0 compilers.
272 The final model run required about 40,000 core hours and the hourly output for all three domains
273 encompasses roughly 3.3 TB of data.

274 For the evaluation, we considered the boxplots for different meteorological variables on
275 an hourly and daily basis. The whiskers comprise 1.5 times the interquartile range. Moreover, we
276 calculated the Pearson correlation between the variables of the COSMO_{iso} output and the Valley
277 Station, except for precipitation, where we used the Spearman correlation, because the data is not
278 normally distributed. From these, we determined the coefficient of determination (R^2) and the
279 significance by their p -values. Furthermore, we calculated the root mean square error (RMSE)

280 and the mean bias. The heights of the COSMO_{iso} output correspond to the heights of the Valley
 281 Station for all variables apart from wind. The COSMO_{iso} wind variable was initially output at
 282 10 m. For comparability with the AWS wind data, the COSMO_{iso} wind was interpolated to 2 m
 283 assuming a logarithmic wind speed profile (Allen et al., 1998).

284 2.4 Rain Type Classification

285 A common approach to distinguish convective and stratiform precipitation is the use of
 286 the Tropical Rainfall Measuring Mission (TRMM) satellite data and algorithm (Aggarwal et al.,
 287 2016; Funk et al., 2013; Schumacher & Houze, 2003). In stratiform regions a so called ‘bright
 288 band’ occurs just below the melting layer and describes a horizontal layer of 500 m thickness
 289 with high radar reflectivity values. In contrast, convective regions are characterized by a
 290 vertically extending core of maximum reflectivity (Houze, 2014). The spatial and temporal
 291 resolution of the TRMM product is, however, too coarse and therefore not suitable for our study.
 292 In GCMs the separation arises from the convection parameterization. This means that all
 293 precipitation calculated within the parametrization scheme is classified as convective and the
 294 explicitly calculated one is classified as stratiform. With increasing spatial resolution, the climate
 295 model can resolve convective processes, leading to a misclassification of convective
 296 precipitation as stratiform rain. Consequently, a specifically tailored separation technique for
 297 stratiform and convective precipitation is needed for high-resolution models. We followed the
 298 approach of Sui et al. (2007) that is based on cloud microphysical processes expressed as ratio of
 299 the integrated ice and liquid water path (IWP and LWP, respectively). Particularly, the cloud
 300 ratio is defined as IWP/LWP, with IWP being the sum of the vertically integrated mixing ratios
 301 of all ice species (Q_{snow} + Q_{ice} in our case), and LWP being the sum of the vertically integrated
 302 mixing ratios of all liquid particles (Q_{cloud} + Q_{Rain}). Consequently, the cloud ratio can be
 303 interpreted as the relative importance of ice and liquid hydrometeors in clouds. Precipitation is
 304 classified as

- 305 • **Convective**, if the cloud ratio is < 0.2 (to account for high rain rates, i.e. high LWP)
 306 or if $IWP > IWP_{\text{threshold}}$ (for particularly high ice contents)
 307 The $IWP_{\text{threshold}}$ is the mean of IWP plus one standard deviation of IWP
 308 (here: $IWP_{\text{threshold}} = 2.31$ mm)
- 309 • **Stratiform**, if the cloud ratio is > 1.0 (to make sure that ice exists, but is related to low rain
 310 rates, i.e. low LWP).
- 311 • **Mixed**, for all remaining precipitation.

312 A distinct, process-based consideration of each class is an essential part of this study,
 313 which is why we additionally separated the convective class into shallow (cloud ratio < 0.2) and
 314 deep ($IWP > IWP_{\text{threshold}}$) convection. A discussion of this nomenclature is included in the results
 315 section (see Section 3.2.2). Sui et al. (2007) regarded the mixed class as belonging to stratiform
 316 rain, which we adopted for our study. Consequently, we refer to the subclasses of stratiform rain
 317 as mixed and strictly stratiform. This rain type classification highlights the importance of ice and
 318 snow with respect to the liquid particles for stratiform precipitation (Sui et al., 2007) (Figure S2
 319 in Supporting Information S1). To evaluate the classification of the rain types, we considered the
 320 distribution of rain rates with respect to their fractional contribution to the overall precipitation
 321 amount (Klingaman et al., 2017).

322 For the stratiform fraction, we followed different other studies (Aggarwal et al., 2016; Hu
323 et al., 2018) and calculated it as fraction of the sum over all rain rates of the stratiform and mixed
324 class to the sum over all rain rates. For very small rain rates the stratiform fraction might be
325 misleading, which is why we only considered hours with a total rain rate > 0.03 mm. Such a
326 threshold is commonly also applied when using the $\delta^{18}\text{O}_\text{P}$ of the COSMO_{iso} output (Pfahl et al.,
327 2012).

328 **3 Results and Discussion**

329 **3.1 Evaluation of COSMO_{iso} and the Rain Type Classification**

330 In the following, we present an evaluation of COSMO_{iso} to ensure a realistic performance
331 of the model regarding the hydrometeorological variables and the stable water isotopes.
332 Thereafter, the classification method for the different rain types is evaluated. For this evaluation,
333 we consider the distributions of rain rate contributions to the overall precipitation amount.

334 **3.1.1 Hydrometeorological Variables**

335 We adjusted the COSMO_{iso} setup and evaluated its output with AWS data of the Valley
336 Station by selecting the closest grid cell to this station. The Mountain Station serves as a
337 reference for the variability that can be expected nearby (for orientation: the closest grid cell to
338 the Mountain Station is two grid cells south and one grid cell west of the closest grid cell to the
339 Valley Station; model output from this grid cell is not used for adjusting the COSMO_{iso} setup and
340 also not for the statistical evaluation). We chose this location at the western flanks of the Andes,
341 because tree ring material for stable isotope analysis were collected close to the Valley Station.
342 In a follow-up study, we want to explain these tree ring signals by using the COSMO_{iso} output.

343 The hourly and daily temperature at 2 m is realistically captured (Figure 2) with a
344 significant correlation and a R^2 of 0.75 for hourly values. It decreases to 0.11 for daily values due
345 to the removal of the daily cycle by the calculation of the mean. However, this temporal
346 aggregation leads to a decrease of the RMSE from 1.7 °C to 1.04 °C from hourly to daily,
347 respectively. The performance resembles the one in other atmospheric modeling studies with a
348 similar setup (convection-resolving, mountain environment, AWS data as observations,
349 simulation period from a few days to a few months). For example, for the complex topography of
350 the New Zealand Alps values for temperature at 2 m of 2.64 °C and 0.88 for the hourly RMSE
351 and the R^2 , respectively, were reported (Kropač et al., 2021). For a study of Foehn in Patagonia,
352 Temme et al. (2020) obtained an hourly RMSE from 1.72 to 3.63 °C (depending on foehn event
353 and AWS site) and a maximum R^2 of 0.77. And for a tropical high mountain in Africa, (Collier
354 et al., 2019) obtained 0.34 for the daily R^2 and a mean deviation (comparable to RMSE) of 0.4
355 °C. Modelled shortwave radiation does not capture the highest observed values, resulting in a
356 RMSE of 157.92 W/m² for hourly values, which is reduced to 53.94 W/m² for daily ones. This is
357 again in accordance with the other studies; in the New Zealand case, the hourly RMSE of
358 incoming shortwave radiation came to 73.94 W/m² (Kropač et al., 2021), while the absolute mean
359 deviation in the Africa study for daily values was 42.8 W/m² (Collier et al., 2019). Temperature
360 at 2 m and shortwave radiation of the Mountain Station considerably differ from those of the
361 Valley Station that is located nearby. This is to be expected in areas of complex topography.
362 However, the fact that COSMO_{iso} realistically reproduces temperature at 2 m and shortwave
363 radiation at the Valley Station in this region of high spatial variability is, therefore, encouraging.

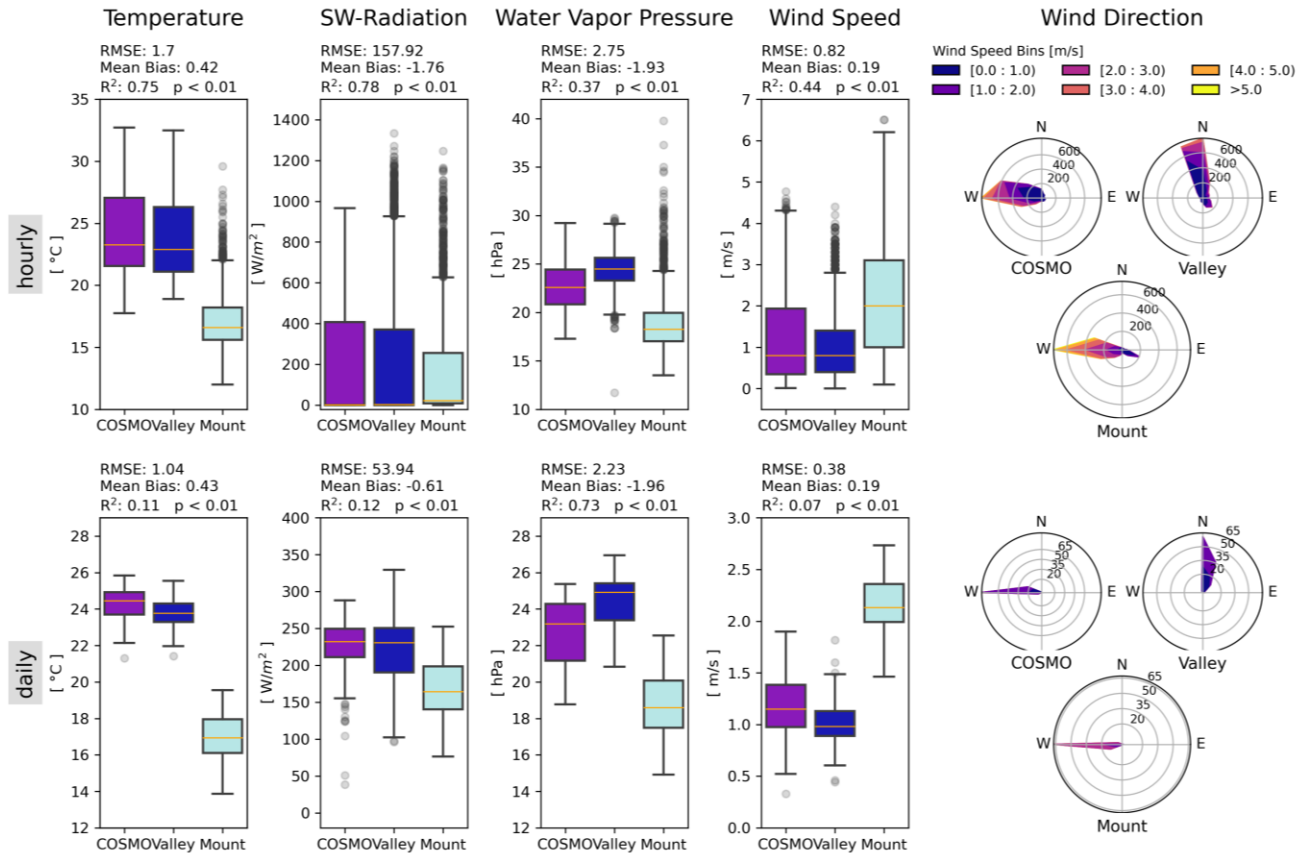


Figure 2. Evaluation of COSMO_{iso} temperature at 2 m (first column), shortwave radiation at the surface (second column), water vapor pressure at 2 m (third column), wind speed at 2 m (fourth column) and wind direction at 2 m (wind roses) against Automatic Weather Station (AWS) data (Valley and Mountain Station) for hourly (upper row) and daily (lower row) values. The Root Mean Square Error (RMSE), Mean Bias and Coefficient of Determination (R²) are calculated between the COSMO_{iso} output and the Valley Station.

364 The humidity expressed as water vapor pressure, is slightly underestimated (mean bias
 365 for daily and hourly about -1.9 hPa) but the mean is clearly closer to the Valley Station than to
 366 the Mountain Station. The mean bias of wind speed is small with 0.19 m/s for both temporal
 367 resolutions and COSMO_{iso} again manages to represent conditions at the Valley Station in a
 368 realistic way, but not the ones at the Mountain Station. While the other studies cited above are
 369 harder to compare for these two variables in terms of absolute values (either because they used
 370 different measures of air humidity, or they decided on a different evaluation strategy for wind
 371 speed concerning the reference height), our metrics lie within their performance ranges for
 372 variability. For example, they demonstrate hourly R² to vary substantially from 0.14-0.72 (0.37
 373 in our case) for humidity (Kropač et al., 2021; Temme et al., 2020), and a maximum of 0.52
 374 (0.44 in our case) for wind speed (Kropač et al., 2021). The wind direction of COSMO_{iso} more
 375 closely resembles that of the Mountain Station, which is caused by the real orientation of the
 376 narrow valley where the Valley Station is located. This topographic condition is not captured by
 377 the spatial resolution of 1.5 km of D3. The same, but understandable, deviation was found in a
 378 very recent study of a high-mountain environment in New Zealand (Kropač et al. 2023, under
 379 review)

380 Precipitation as the focus variable of this study shows a good performance as well
 381 (Figure 3), in particular cumulative precipitation amounts align well with the Valley Station. The
 382 R^2 of hourly precipitation is expectedly low, since the exact timing of precipitation events
 383 typically differs between models and observations at such high temporal resolution (e.g., Mölg &
 384 Kaser, 2011). However, the R^2 of daily precipitation of 0.28 is even slightly better than the ones
 385 for a high-resolution model simulation over Ecuador, yielding a R^2 of 0.05 and 0.2 for an AWS
 386 at the coast and one at 2685 m altitude, respectively (Chimborazo & Vuille, 2021). Nevertheless,
 387 the promising and important aspect in the results is that high intensity precipitation events are
 388 realistically reproduced in terms of both rain rate and duration. Furthermore, the daily cycle is
 389 well captured. A study over the European Alps covering ten years found a similarly high
 390 agreement in the daily cycle (Ban et al., 2014). They could show that it resulted from the explicit
 391 representation of convection in a high-resolution setup with COSMO. However, between 9 p.m.
 392 and 1 a.m. local time, precipitation is slightly overestimated in our model, and it is slightly
 393 underestimated in the morning hours.

394 To evaluate the spatial hydroclimatic variability of the $\text{COSMO}_{\text{iso}}$ output, we compared
 395 the column water-vapor amounts provided by the MODIS precipitable water product to the time
 396 mean of the vertically integrated water vapor (TQV) from $\text{COSMO}_{\text{iso}}$ (Figure 3). It can be
 397 noticed that humidity is underestimated in the coastal regions. This is in accordance with the

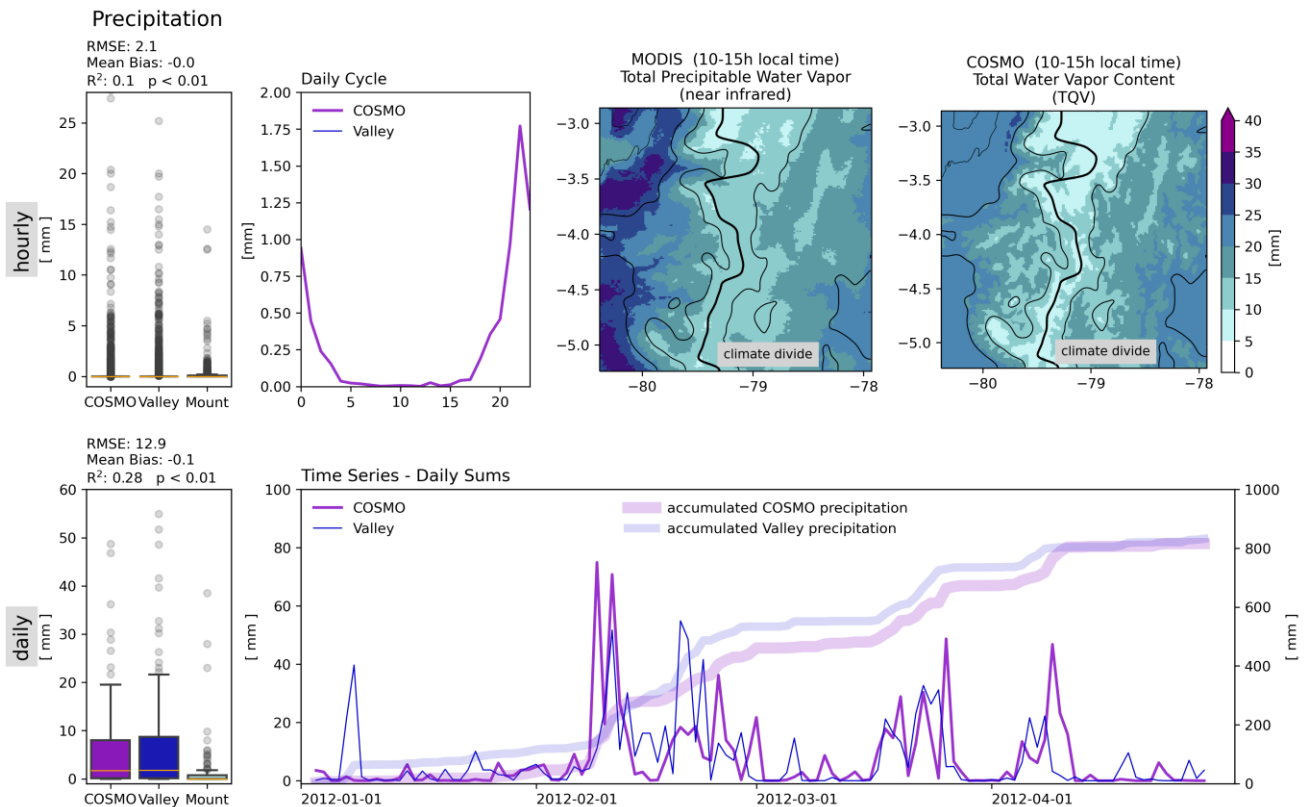


Figure 3. Evaluation of precipitation from $\text{COSMO}_{\text{iso}}$ against AWS data considering boxplots of hourly and daily sums (upper and lower panel of first column, respectively), the daily cycle (upper panel of second column) and accumulated precipitation amounts (lower panel). Spatial evaluation of total water vapor content against satellite retrievals from the MODerate resolution Imaging Spectroradiometer (MODIS) (upper right panels). The RMSE, Mean Bias and R^2 are calculated between the $\text{COSMO}_{\text{iso}}$ output and the Valley Station.

398 slight underestimation of humidity observed in comparison with the Valley Station. A similar
 399 underestimation of specific humidity is also found in a series of simulations over the North
 400 Atlantic trade wind region (Villiger et al., 2023). The Andes and the topographic effects are,
 401 however, well captured, giving confidence in the simulated spatial pattern. Accordingly, the
 402 spatial correlation coefficient amounts to 0.52 (p -value < 0.01).

403 3.1.2 Stable Oxygen Isotopes of Precipitation

404 Isotopic data are scarce in the vicinity of the study site and only available with a monthly
 405 resolution. Therefore, we conducted the evaluation separately for every model domain (D1, D2,
 406 D3). The monthly mean $\delta^{18}\text{O}_P$ of COSMO_{iso} realistically captures the depleted signal with
 407 increasing altitude and the only slightly depleted values of central America, a result included in
 408 Figure 1 to re-call the topographic conditions of the study region. The amount effect in
 409 COSMO_{iso}, meaning the relationship between the hydroclimate and the stable water isotope
 410 signals, is well reproduced, which is shown by the significant daily negative correlation between
 411 daily rain sums and daily mean $\delta^{18}\text{O}_P$ (Figure S3 in Supporting Information S1).

412 3.1.3 Rain Type Classification

413 The distribution of the precipitation contribution of stratiform and convective rain rates to
 414 the total rain amount shows a maximum of the distribution of the stratiform rain rates being
 415 clearly smaller than the convective one (Figure 4a). Breaking down the classification further into
 416 strictly stratiform, mixed, shallow and deep convection (Figure 4b) emphasizes the distinct rain
 417 rate difference between deep convection and strictly stratiform rain even more. The mixed rain
 418 rates are, as expected, mostly between deep convective and strictly stratiform. The shallow
 419 convection maximum rain rates occur at lower rain rates than deep convective ones and slightly
 420 higher than mixed ones. Further confirmation for this partition method is included within the
 421 main analysis (see Section 3.2.2). Overall, the results confirm the usefulness of this classification
 422 scheme to distinguish between the different rain formation pathways.

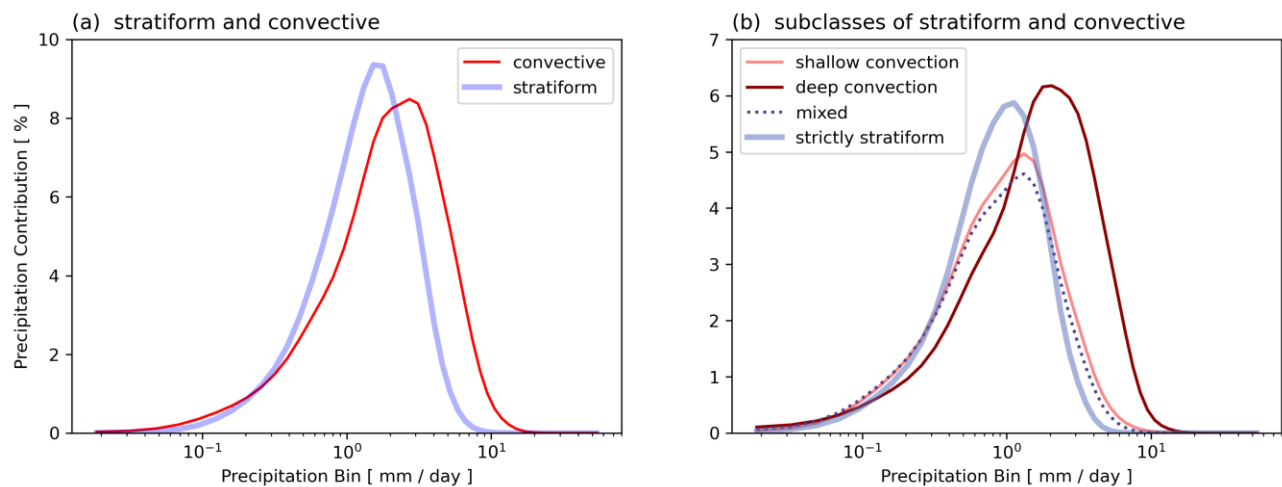


Figure 4. Contribution of each rain rate bin to the total precipitation of each rain type: convective and stratiform rain (a) and their subclasses (b). The area below each curve sums up to 100 %.

423 3.2 Relationship Between $\delta^{18}\text{O}_\text{P}$ and Rain Types

424 The main analysis starts with the consideration of the relationship between stratiform
 425 fraction and $\delta^{18}\text{O}_\text{P}$ based on model output of COSMO_{iso}. This is followed by a thorough
 426 investigation of the underlying processes and ends with an analysis of the variability of the
 427 occurrence of rain types in time and a suggestion for using a deep convective fraction or shallow
 428 convective fraction due to the large difference in their associated isotope signals.

429 3.2.1 Correlation Between $\delta^{18}\text{O}_\text{P}$ and Stratiform Fraction

430 The regression slope of the correlation between daily stratiform fraction and daily mean
 431 $\delta^{18}\text{O}_\text{P}$ shows a distinct east-west pattern (Figure 5a) with a negative relationship west and a
 432 positive relationship east of the climate divide. The regression slopes are significant
 433 (p -values < 0.05) only in a few regions (Figure 5b). Thereby, we additionally accounted for field
 434 significance (i.e., for spatial autocorrelation) by minimizing the false discovery rate (FDR)
 435 (Wilks, 2011). The latter strongly decreased the area of significant correlations (not shown). The
 436 R^2 (Figure 5c) is higher west of the climate divide than on the eastern side. Overall, the R^2 values
 437 are not particularly high, only a few are above 0.4. On the one hand, the small number of
 438 significant grid cells and the low R^2 values probably arise from the high temporal resolution
 439 (daily). The same observation has been made for the amount effect, which shows a similar
 440 reduced explained variance with an increased temporal resolution (Risi et al., 2008; Vimeux et
 441 al., 2005). On the other hand, the spatial extent the stratiform fraction is calculated for, is another
 442 factor. For example, Aggarwal et al. (2016) determined the stratiform fraction for a box of about
 443 275 km x 275 km, whereas in our study, it is calculated for each grid cell (1.5 km x 1.5 km). In
 444 fact, we achieved the highest R^2 using a region-wide stratiform fraction (not shown) and

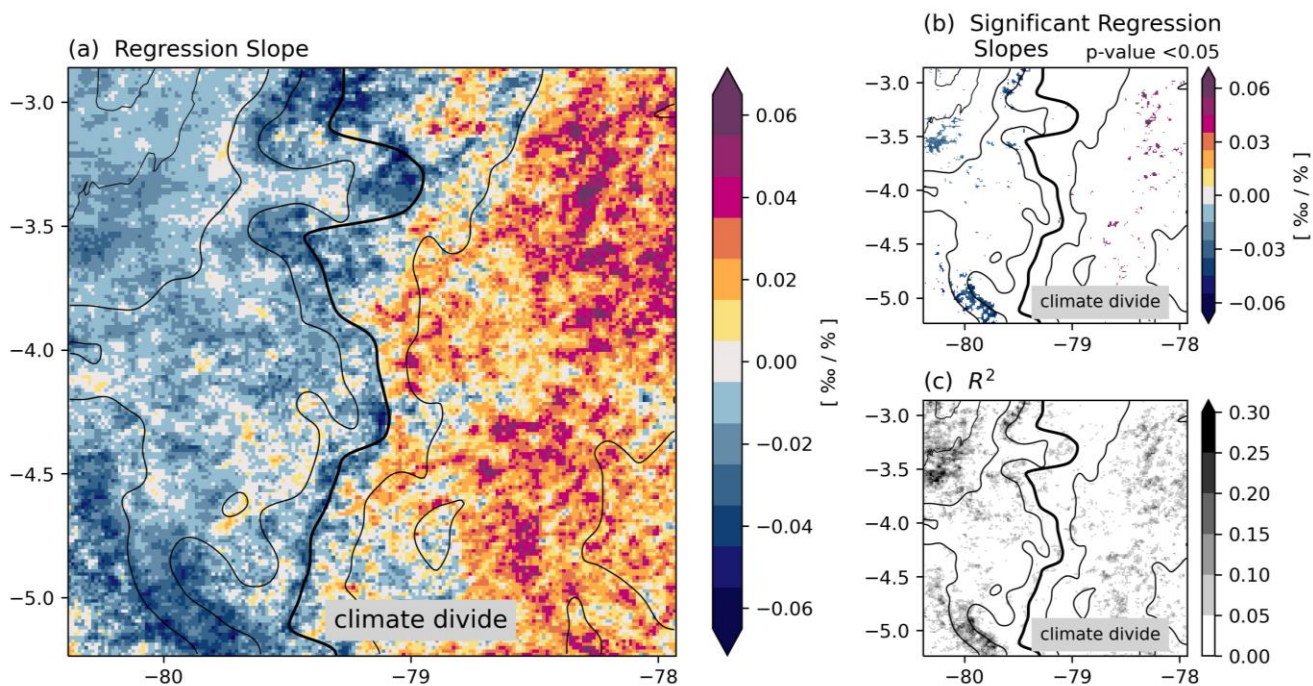


Figure 5. Regression slope between $\delta^{18}\text{O}_\text{P}$ and the stratiform fraction (a), significant regression slopes (p -value < 0.05 and additionally accounted for field significance by minimizing the false discovery rate) (b) and R^2 of the correlation (c).

445 similarly, Vargas et al. (2022) found the best correlation with $\delta^{18}\text{O}_p$ using region-wide
 446 precipitation. However, for a better understandability, we used the grid-cell-based calculation of
 447 the stratiform fraction.

448 The negative relationship west of the climate divide is consistent with a tropical to mid-
 449 latitude wide observational study using monthly GNIP station $\delta^{18}\text{O}_p$ and TRMM based stratiform
 450 fractions (Aggarwal et al., 2016). A site-specific and daily analysis covering tropical and
 451 subtropical stations further confirms this relationship (Munksgaard et al., 2019). The latter study,
 452 however, also encompasses a few stations showing a positive relationship. Generally, all stations
 453 of their study are influenced by a maritime climate, and the few continental sites were excluded
 454 from the main analysis, because of a weak relationship. Our hypothesis is that the stratiform
 455 fraction is not a good measure of rainfall formation pathways in this region. As convection is the
 456 main driver for tropical precipitation with stratiform precipitation being a consequence (MCS),
 457 we need to look closer into the different rainfall formation pathways.

458 3.2.2 Seasonal Mean Analysis

459 In search for the reason for the differing regression sign east and west of the climate
 460 divide for the relationship between the stratiform fraction and $\delta^{18}\text{O}_p$, we analyzed seasonal mean
 461 composites of different atmospheric variables. The composites are based on the rain types
 462 convective and stratiform as well as on their subclasses deep convective, shallow convective,
 463 strictly stratiform and mixed rain (see Section 2.4).

464 To eliminate the influence of the topography on the $\delta^{18}\text{O}_p$, which leads to a decrease of

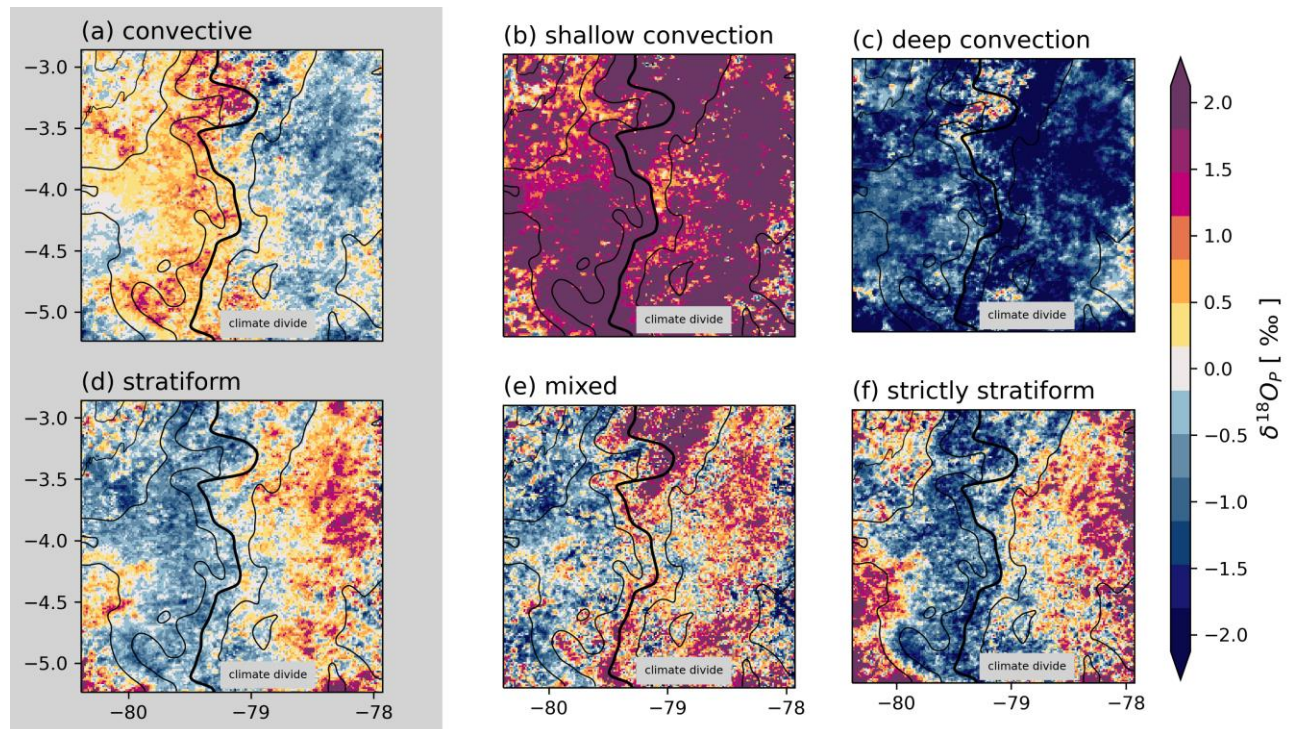


Figure 6. Seasonal mean anomaly composites of $\delta^{18}\text{O}_p$ for convective and stratiform rain ((a) and (d), respectively, grey background) and their subclasses shallow convection, deep convection, mixed and strictly stratiform ((b),(c),(e) and (f), respectively, white background).

465 $\delta^{18}\text{O}_P$ with altitude (Dansgaard, 1964) that would dominate the composite, we subtracted the
 466 mean over all “rainy” time steps (hours with rain >0 mm) at each grid point from the seasonal
 467 mean $\delta^{18}\text{O}_P$ at the respective grid point. This procedure is restricted to the rainy time steps, as the
 468 seasonal mean composites for each rain type, by definition, only considers rainy time steps at
 469 each grid cell. In the following, we refer to the $\delta^{18}\text{O}_P$ composite as anomaly composites and to
 470 the seasonal mean composites just as composites.

471 The $\delta^{18}\text{O}_P$ anomaly composites for convective and stratiform rain (Figure 6a and 6d,
 472 respectively) show a very similar east-west dipole pattern as the sign of the regression between
 473 stratiform fraction and $\delta^{18}\text{O}_P$ (Figure 5). Revealing the reason for the $\delta^{18}\text{O}_P$ pattern for the
 474 convective and stratiform composites will help to understand the contrasting signs in the
 475 stratiform fraction- $\delta^{18}\text{O}_P$ relationship. The convective (first row (a-c) of Figure 6 to Figure 11)
 476 and stratiform (second row (d-f) of Figure 6 to Figure 11) formation pathway will be examined
 477 separately and in more detail in the next two sections.

478 3.2.2.1 Mechanisms Driving the Convective $\delta^{18}\text{O}_P$

479 The $\delta^{18}\text{O}_P$ anomaly composite of shallow and deep convection (Figure 6b and 6c,
 480 respectively) shows a markedly distinct signal of relatively enriched and depleted $\delta^{18}\text{O}_P$ values,
 481 respectively. In the following, we show that these differences do not only arise due to the rain
 482 type definition itself but can also be physically constrained.

483 Positive vertical velocities for deep convection (Figure 7c) are reaching from a few
 484 kilometers above the surface to an altitude of almost 15 km. Whereas, for shallow convection
 485 (Figure 7b), they hardly reach beyond the atmospheric melting layer. The latter is indicative for
 486 the predominant occurrence of the cloud types shallow cumulus and cumulus congestus.
 487 Together with cumulonimbus, they make up the three dominating cloud types of the tropics.
 488 Shallow cumuli and cumuli congestus reach up to heights of about 2 km and near the
 489 atmospheric melting layer, respectively, and consist only of liquid particles (Johnson et al.,

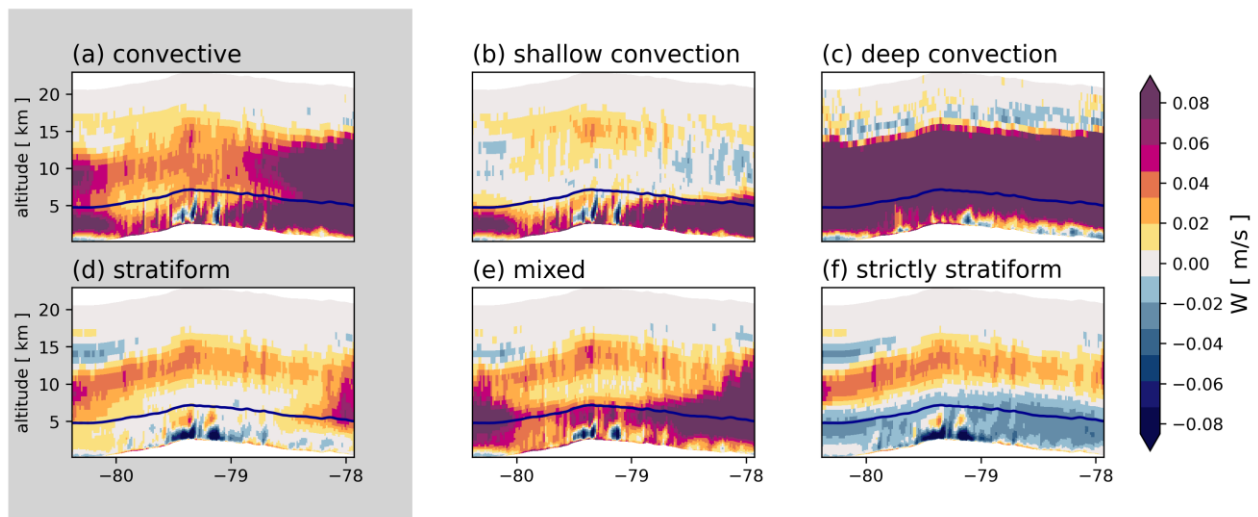


Figure 7. Seasonal meridional mean of vertical velocity for convective and stratiform rain ((a) and (d), respectively, grey background), their subclasses shallow convection, deep convection, mixed and strictly stratiform ((b),(c),(e) and (f), respectively, white background) and the seasonal meridional mean height of the atmospheric melting layer ($T=0^\circ\text{C}$, bold line).

490 1999). This is consistent with the IWP composite (Figure S4 in Supporting Information S1),
 491 which is, by rain type definition, very low for shallow convection and very high for deep
 492 convection. In contrast, the LWP composite is high for both convective rain types; hence,
 493 leading to high rain rates (Figure S5 in Supporting Information S1). For simplicity, we use the
 494 term shallow convection, although it also comprises mid-level convection of cumuli congestus.

495 Low outgoing longwave radiation (OLR) at the top of the atmosphere, as an indicator for
 496 deep convection (Gao et al., 2013; Wang, 1994; Wang & Xu, 1997), mirrors the $\delta^{18}\text{O}_p$ anomaly
 497 composite of shallow and deep convection. As one would expect, very low OLR values are
 498 associated with deep (Figure 8c) and high OLR values coincide with shallow convection (Figure
 499 8b).

500 Linking the $\delta^{18}\text{O}_p$ anomaly composite with the vertical velocity, IWP, LWP and OLR
 501 composites, shows that the $\delta^{18}\text{O}_p$ signals can be explained by differing microphysical and
 502 dynamical mechanisms. Additionally, this further increases the confidence in the rain type
 503 partitioning method. Hence, it is reasonable to conclude from the synthesis of data that shallow
 504 convection is related to relatively enriched $\delta^{18}\text{O}_p$ signals, whereas deep convection is related to
 505 highly depleted $\delta^{18}\text{O}_p$ values.

506 To explain the differing sign of $\delta^{18}\text{O}_p$ signals east and west of the climate divide for
 507 convective rainfall (Figure 6a), we calculated the fractional contribution of each class and
 508 subclass to the total seasonal precipitation amounts at each grid cell (Figure 9). West of the
 509 climate divide, shallow convection mostly contributes to seasonal precipitation amounts (Figure
 510 9b), whereas east of the climate divide, it is the deep convection (Figure 9c). In this respect, it is
 511 noteworthy, that a little patch exists west of the climate divide that does have a high contribution

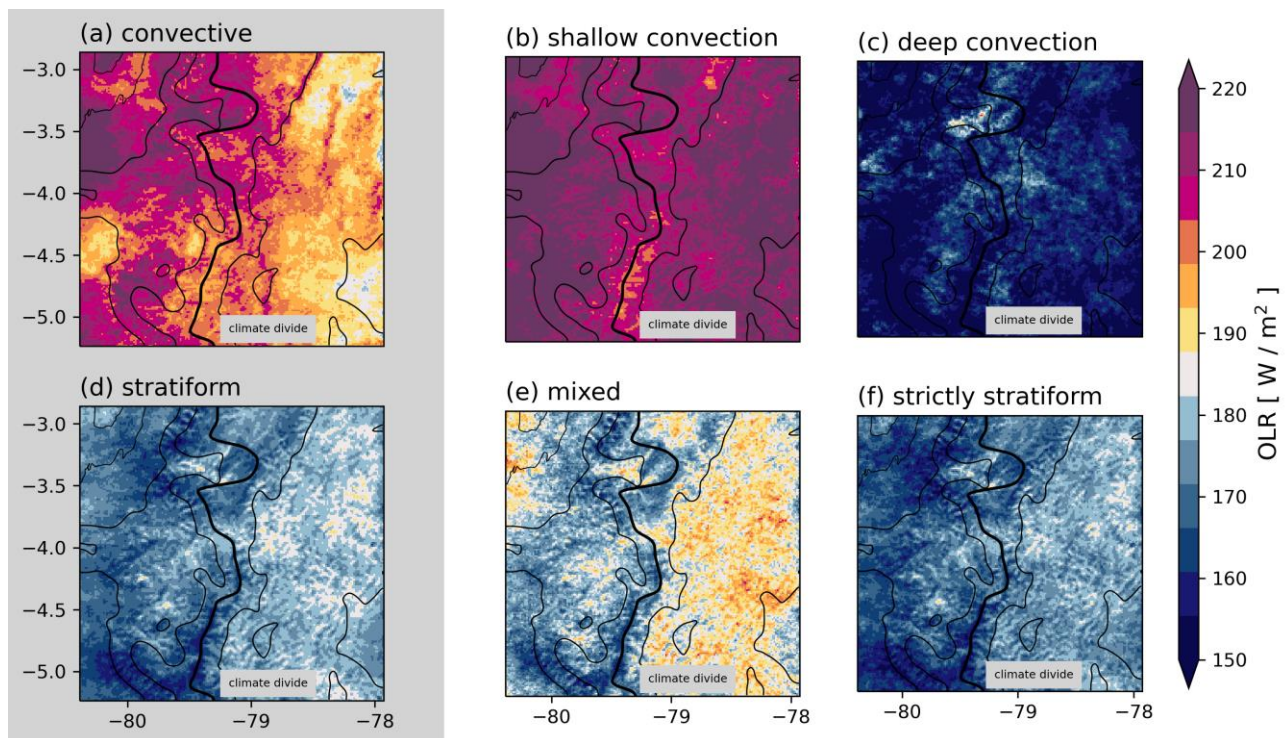


Figure 8. Seasonal mean composites of outgoing longwave radiation (OLR) for convective and stratiform rain ((a) and (d), respectively, grey background) and their subclasses shallow convection, deep convection, mixed and strictly stratiform ((b),(c),(e) and (f), respectively, white background).

512 from deep convection (Figure 9c). This is linked to an increasing elevation acting as a trigger for
 513 deep convection. Overall, we conclude that the relatively enriched $\delta^{18}\text{O}_\text{P}$ signal in most areas
 514 west of the climate divide arises mainly from the dominant contribution of shallow convection to
 515 seasonal precipitation amounts whereas the depleted signal east of it reflects the prevailing
 516 influence of deep convection.

517 The western lowlands and western flanks are in the vicinity of the Pacific Ocean,
 518 therefore, it is not surprising that shallow convection is quite pronounced as it is mainly an
 519 oceanic phenomenon (Houze et al., 2015; Lacour et al., 2018). In contrast, deep and intense
 520 convection occurs prevalently over land (Houze et al., 2015) and leads to rather low water
 521 isotope signals east of the climate divide.

522 3.2.2.2 Mechanisms Driving The Stratiform $\delta^{18}\text{O}_\text{P}$

523 The opposed west-east $\delta^{18}\text{O}_\text{P}$ gradient in the anomaly composite pattern of stratiform
 524 precipitation (Figure 6d), compared to the gradient in the $\delta^{18}\text{O}_\text{P}$ of convective precipitation,
 525 cannot be explained by differences in the $\delta^{18}\text{O}_\text{P}$ signal or the precipitation contribution between
 526 mixed and strictly stratiform. A slight difference in OLR with lower OLR values in the west
 527 (Figure 8f) coincide with and can be explained by enhanced upward velocities above the
 528 atmospheric melting layer in the west (Figure 7f). The latter together with the descending motion
 529 below the atmospheric melting layer is characteristic of stratiform circulation properties (Houze,
 530 2014).

531 However, the different contributions of shallow and deep convection in the west and in

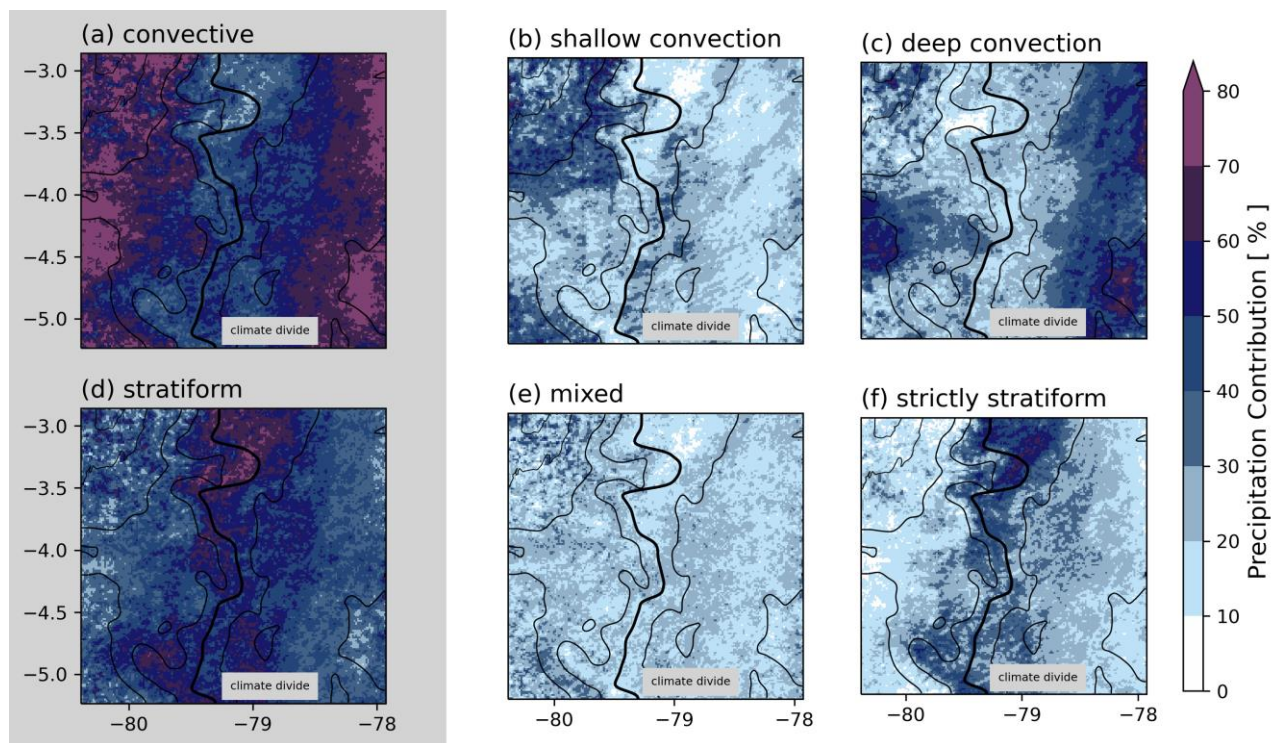


Figure 9. Precipitation contribution to seasonal precipitation amounts for convective and stratiform rain ((a) and (d), respectively, grey background) and their subclasses shallow convection, deep convection, mixed and strictly stratiform ((b),(c),(e) and (f), respectively, white background).

532 the east of the climate divide are more important in this context. In particular, west of the climate
 533 divide, where shallow convection is most pronounced, the intense relative enriching effect of
 534 shallow convection results in a relatively positive $\delta^{18}\text{O}_p$ sign for convective precipitation (Figure
 535 6a) and consequently to a negative sign for stratiform precipitation, which in this region tends to
 536 originate from relatively higher altitudes than the shallow convective precipitation (Figure 6d).
 537 East of the climate divide, where deep convection dominates over shallow convection, this
 538 relationship is reversed (stratiform precipitation tends to originate from relatively lower altitudes
 539 than in deep convective systems). In the following section, we will show that the rate of
 540 depletion from stratiform precipitation is not dependent on the region, which in turn gives
 541 evidence of the described effect of the differing shallow and deep convective contributions west
 542 and east of the climate divide.

543 3.2.3 Strength of the Amount Effect

544 To clarify which rain type yields the highest depletion with rain rates, we analyzed the
 545 strength of the amount effect for each rain type. Therefore, we calculated the regression slope
 546 (Figure 10) and the R^2 (Figure S6 in Supporting Information S1) between hourly rain rate and
 547 hourly $\delta^{18}\text{O}_p$ at each grid cell for each rain type, separately. Only regression slopes smaller than -
 548 1 ‰/mm are statistically significant (p -values smaller than 0.05 and additionally accounting for
 549 field significance with the FDR approach, Figure S7 in Supporting Information S1). The
 550 depleting effect for shallow convection is the weakest (Figure 10b) and the one for deep
 551 convection (Figure 10c) is the most intense followed by mixed rain (Figure 10e). The amount
 552 effect for strictly stratiform (Figure 10f) is weaker than that for deep convection and over wide

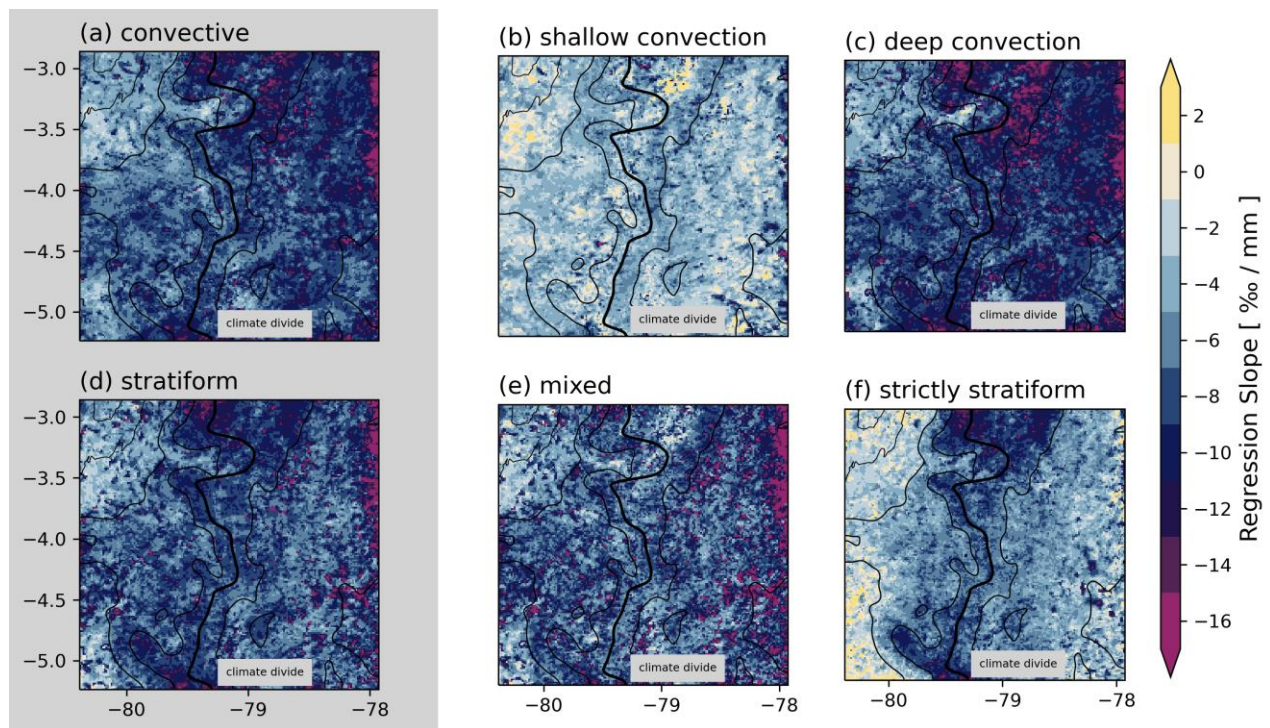


Figure 10. Strength of the amount effect – regression slope between $\delta^{18}\text{O}_p$ and hourly rain rates for convective and stratiform rain ((a) and (d), respectively, grey background) and their subclasses shallow convection, deep convection, mixed and strictly stratiform ((b),(c),(e) and (f), respectively, white background).

553 areas closer to shallow convection. Comparing the classes of convective (Figure 10a) and
 554 stratiform precipitation (Figure 10d) does not show a pronounced difference although clear
 555 differences arise within the subclasses. Moreover, the depleting effect of each rain type is
 556 spatially relatively uniform and independent of the region, supporting our assumption of the
 557 effect of the relative contributions of shallow and deep convection in the west and in the east of
 558 the climate divide on the stratiform anomaly composite of $\delta^{18}\text{O}_p$ (Figure 6d, see Section 3.2.2.2).

559 3.2.4 Influence of Rain Types on D-Excess

560 In addition to the results above focusing on $\delta^{18}\text{O}_p$, we considered seasonal mean
 561 composites of d-excess, which may reveal non-equilibrium effects like vapor deposition on ice in
 562 supersaturated conditions or sub-cloud rain evaporation (Figure 11). For all rain types a west-east
 563 gradient is evident with values between -5 and 15 ‰ in the west and values greater than 15 ‰ in
 564 the east, which most likely originate from the contrasting moisture source regions. West of the
 565 climate divide, the oceanic influence from the Pacific is of particular importance and leads to d-
 566 excess values of roughly 10 ‰. While the values are higher east of the climate divide, due to
 567 moisture recycling (Aemisegger et al., 2014; Ampuero et al., 2020; Fröhlich et al., 2008) that is a
 568 prominent feature within the Amazon region (Ampuero et al., 2020; Victoria et al., 1991; Zhiña
 569 et al., 2022). An altitude effect, reflecting the topography of the Andes, as found in other study
 570 regions (Gonfiantini et al., 2001; Natali et al., 2022) is not clearly detectable.

571 A striking feature of the d-excess composites is the exceptional high values for deep
 572 convection over the whole area (Figure 11c). The few lower d-excess values within the deep
 573 convection composite come from little rain amounts and hence precipitation contribution of less
 574 than 10 % (Figure 9) and are not representative. However, the effect of deep convective systems

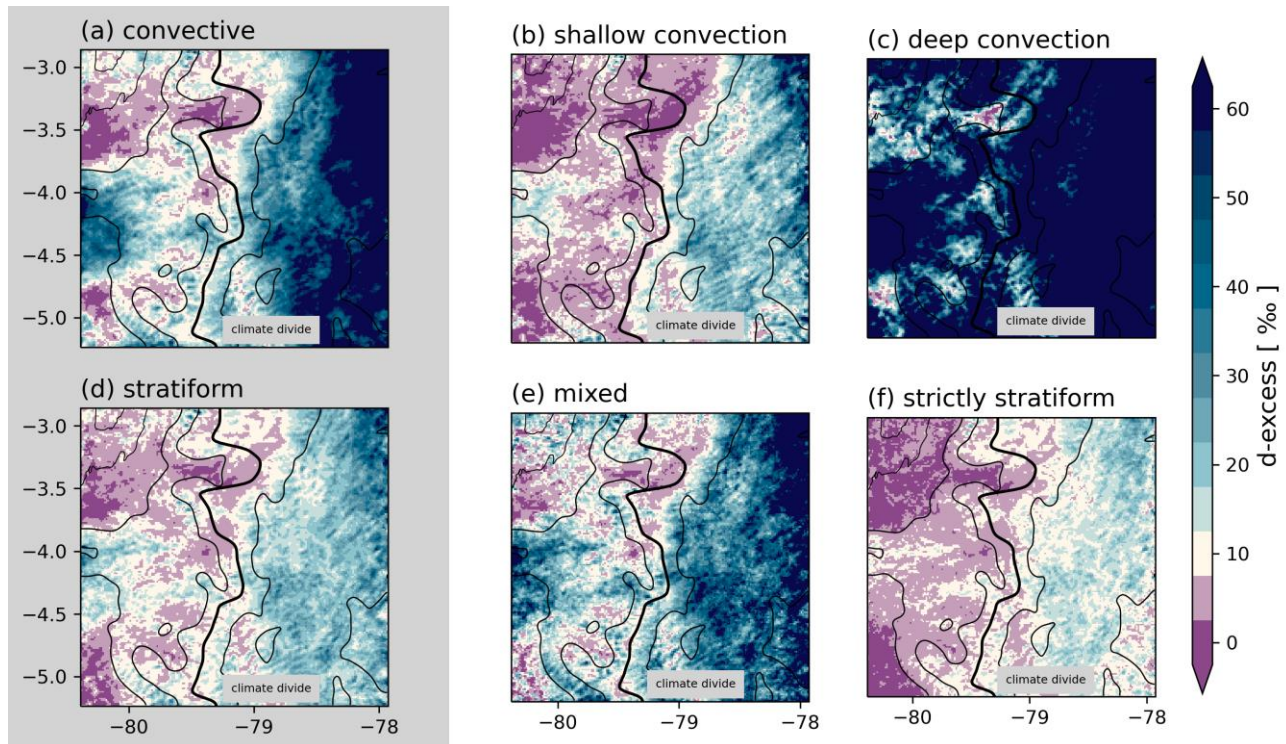


Figure 11. As Figure 8, but for deuterium excess (d-excess).

575 is superimposed to the effect of moisture sources. This can be seen by the region of slightly
576 higher elevation west of the climate divide (at the left border of the map at -4.0°N to -4.5°N). It
577 has high precipitation contributions from deep convection (Figure 9) and is related to high d-
578 excess values despite its close location to the Pacific (Figure 11a and Figure 11c). This finding
579 highlights the importance of the rain formation pathway on the d-excess value of precipitation
580 and is further confirmed by the lowest d-excess values for the strictly stratiform composite.

581 In the following, we comprehensively discuss the $\delta^{18}\text{O}_p$ and d-excess relationship for the
582 different rain types based on the results of the composite analysis and the amount effect in more
583 detail. The contrasting isotopic signal of shallow and deep convection was also found within
584 isotopic water vapor observations covering the Indian Ocean as far as the eastern Pacific (Lacour
585 et al., 2018). Moreover, a sensitivity study with the global isoCAM3.0 at a spatial resolution of
586 155 km agrees with our results and shows that the strength of deep convection is related to the
587 degree of $\delta^{18}\text{O}_p$ depletion (Tharammal et al., 2017). This can be explained by the effect of the
588 strength of convergence (Moore et al., 2014) and a depleting effect with increasing altitude
589 (altitude effect). The latter can be attributed to the removal of condensate by precipitation. As a
590 consequence, the subsequent condensate forms from already depleted vapor (Dansgaard, 1964)
591 and implies that the deeper and higher convective processes reach, the more depleted the $\delta^{18}\text{O}_p$
592 signal becomes. This altitude effect is further supported by the high d-excess values of deep
593 convection, as d-excess of water vapor increases with altitude to values of 150 - 250‰ in the
594 upper troposphere (Bony et al., 2008; Samuels-Crow et al., 2014). Moreover, we suggest that the
595 existence of atmospheric ice and snow is of particular importance for the depletion of $\delta^{18}\text{O}_p$, as
596 deep convection is related to the highest ice and snow contents in our study. Indeed, the
597 fractionation for vapor-to-ice phase changes is higher than for vapor-to-liquid ones (Ciais &
598 Jouzel, 1994; de Vries et al., 2022). Moreover, additional fractionation occurs, when the air is
599 supersaturated over ice, but not over liquid water (supercooled water). In this case, evaporation
600 occurs on supercooled water droplets, while its evaporate deposits on already existing ice
601 crystals. This supersaturation mechanisms is related to non-equilibrium effects (Ciais & Jouzel,
602 1994; Korolev et al., 2017). As d-excess is an indicator for non-equilibrium fractionation, its
603 high values for deep convection (Figure 11c) support our assumption of the importance of ice
604 and snow for the depletion of deep convective precipitation. In contrast, shallow convection
605 consists only of liquid water and the respective cloud tops are not reaching high altitudes
606 explaining the lower depletion of shallow convection.

607 The less intense depletion rate of stratiform rain particularly in contrast to deep
608 convection only partially agrees with other studies. Observational and modeling studies with a
609 coarsely resolved GCM and a conceptual model showed a maximum depletion, when the extent
610 of the stratiform area in a convective system yielded the greatest extent (Kurita, 2013; Kurita et
611 al., 2011). These seemingly contradicting results can be reconciled by the given fact that the
612 maximum in the stratiform area can be explained by a maximum in the intensity of deep
613 convection. As they did not particularly distinguish into stratiform and convective precipitation,
614 this seems plausible. That it is a matter of the same processes is reinforced by a maximum in
615 d-excess accompanying the strongest $\delta^{18}\text{O}_p$ depletion in their and our results. In our strictly
616 stratiform case we assume that sub-cloud rain evaporation does increase the $\delta^{18}\text{O}_p$ value
617 (Aemisegger et al., 2015; Lee & Fung, 2008). This is supported by very low seasonal mean
618 d-excess values of strictly stratiform precipitation that are caused by the decreasing effect on the
619 d-excess value of precipitation during sub-cloud rain evaporation (Fröhlich et al., 2008). In

620 summary, analyzing the effect of rain types on the $\delta^{18}\text{O}_\text{P}$ signal requires the consideration of
621 subclasses and particularly, a separation between shallow and deep convection is necessary.

622 3.3 Occurrence of Rain Types in Time

623 To investigate the temporal evolution of the proportions of rain types to derive a
624 foundation for future studies (e.g. Paleo-isotopic reconstructions), we analyzed the fractional
625 contribution of each rain type to the daily sum of precipitation for the defined regions (see
626 Section 2.1 and Figure S1 in Supporting Information S1): western lowlands, western flanks,
627 Andes and Amazon (Figure 12). It clearly shows that west of the climate divide, the start of the
628 rainy season occurs at the beginning of February and distinct high intensity precipitation events
629 occur besides low amount precipitation events. This agrees well with other studies for tropical
630 high mountains in South America (Bendix & Lauer, 1992; Emck, 2008; Garcia et al., 1998;
631 Landshuter et al., 2020).

632 In contrast, the Amazon reveals rain events with similar intensities that frequently occur
633 throughout the analyzed time period, which is consistent with observations (Garcia et al., 1998).
634 However, the slightly higher precipitation amounts during March and April east of the climate
635 divide (Emck, 2008; Garcia et al., 1998) are not detectable in our study and might be related to
636 the short analysis time period.

637 In all regions, high proportions of shallow convection are associated with low daily rain
638 amounts. Whereas great proportions of stratiform rain co-occur with deep convective ones and
639 can be interpreted as embedded in MCSs. MCSs are a common phenomenon within the study
640 site, irrespective of west or east of the climate divide (Bendix et al., 2003; Bendix et al., 2009;
641 Campozano et al., 2018; Rollenbeck & Bendix, 2011; Zhiña et al., 2022).

642 High proportions of shallow convection are associated with more relatively enriched
643 $\delta^{18}\text{O}_\text{P}$ values. The $\delta^{18}\text{O}_\text{P}$ decreases, particularly, with the occurrence of MCSs. This is consistent
644 with a variety of studies (Garcia et al., 1998; Kurita, 2013; Kurita et al., 2011; Lekshmy et al.,
645 2014; Zwart et al., 2016) and our results (see Section 3.2.2). The western regions show that after
646 a MCS depletion event the $\delta^{18}\text{O}_\text{P}$ recovers to its seasonal mean state at around 0 ‰. In the
647 Amazon, this recovery process is overlapped by a continuous depleting trend in the course of the
648 rainy season, related to the high frequency of rain events. Towards the end of the rainy season, in
649 the beginning of April, this trend is emphasized by a remarkably depleting MCS event
650 comprising an exceptionally high fraction of deep convection. This further confirms our result
651 that particularly deep convection leads to the highest $\delta^{18}\text{O}_\text{P}$ depletion.

652 As MCSs are associated with a high fraction of stratiform rain, it is reasonable to use the
653 stratiform fraction as representative of MCS activity and as depleting parameter. However, our
654 study showed that strictly stratiform rain shows only weak to moderate depletion rates, which is
655 why the use of the stratiform fraction for the rate of depletion might be misleading. Moreover,
656 deep and shallow convection with their opposing $\delta^{18}\text{O}_\text{P}$ effects are classified into the same
657 category within the classical definition of the stratiform fraction. This leads to ambiguity in using
658 the stratiform fraction for the interpretation of stable isotopes.
659

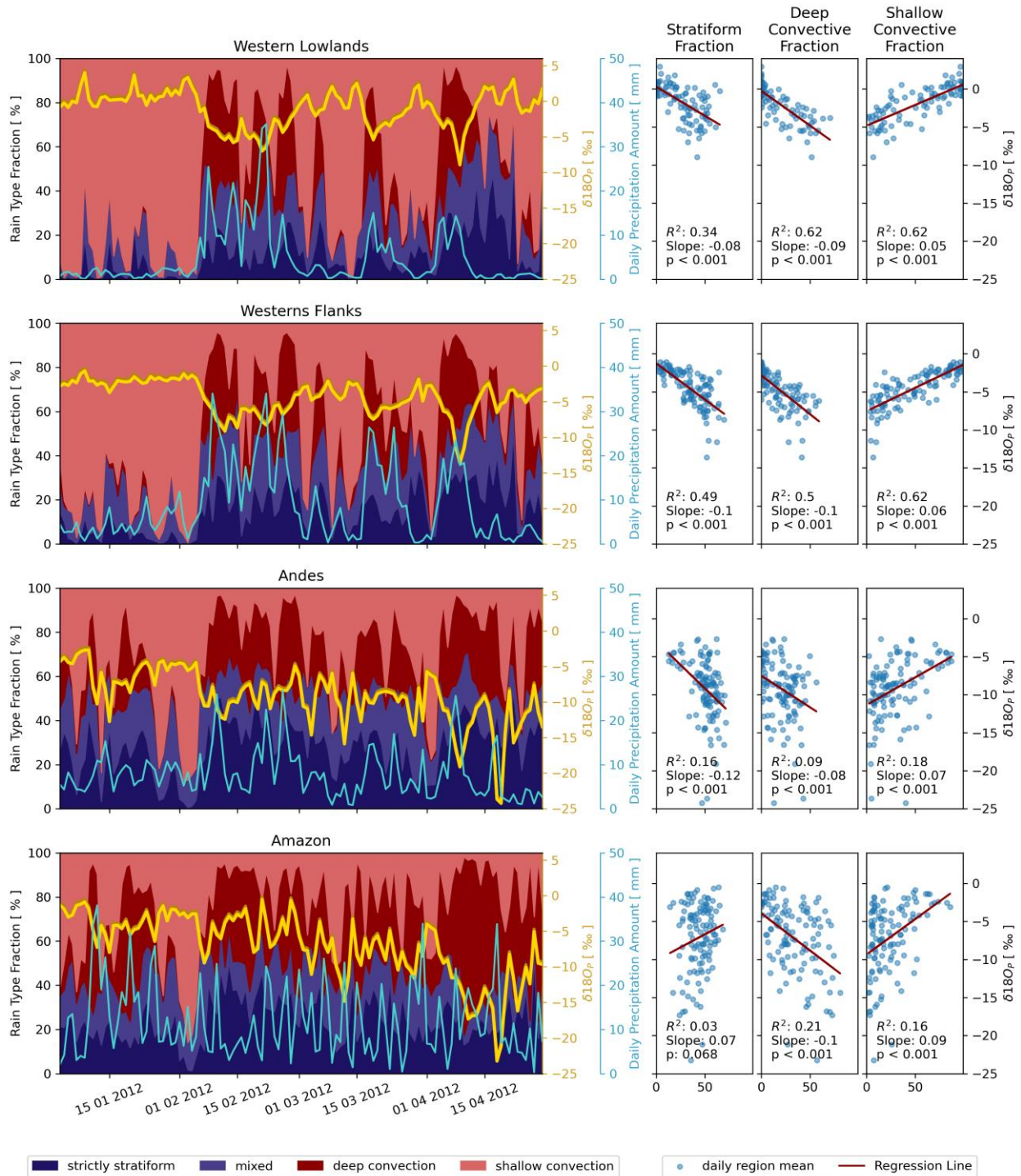


Figure 12. Time series of proportions of rain types (first column) for the different regions (rows) with daily mean $\delta^{18}O_p$ (yellow with darkyellow shadow) and the daily rain sums (cyan). Regression and the respective scatter plot between daily $\delta^{18}O_p$ and the stratiform fraction, deep convective fraction, and shallow convective fraction (second, third and last column, respectively).

3.4 Introduction of the Deep Convective Fraction and the Shallow Convective Fraction

The differing strengths in $\delta^{18}\text{O}_p$ depletion for the rain types demands a reconsideration of the stratiform fraction. As the fraction of deep convection seems to have the greatest influence on the $\delta^{18}\text{O}_p$ signal we suggest the use of a

$$\text{deep convective fraction} = \frac{P_{\text{deep}}}{P_{\text{all}}}$$

with daily rain sums for deep convective rain over a particular region (P_{deep}) and all daily rain sums over the same region (P_{all}). Deep convection occurs beside strictly stratiform and mixed rain in MSCs. All three rain types comprise snow and/or ice, which does not always allow a clear separation when using different techniques. In contrast, shallow convection is easily distinguishable due to its predominantly liquid content and it shows the least depletion rate. Therefore, we alternatively suggest a shallow convective fraction

$$\text{shallow convective fraction} = \frac{P_{\text{shallow}}}{P_{\text{all}}}$$

with daily rain sums for shallow convective rain over a particular region (P_{shallow}).

Using these two definitions for the correlation with $\delta^{18}\text{O}_p$ yields an increased R^2 in contrast to the stratiform fraction (Figure 12). This particularly applies for the western lowlands, where the R^2 rises from 0.34 for the stratiform fraction to 0.62 for the deep and shallow convective fraction. The western flanks and the Andes do yield moderate improvements, and one slight decrease in the strength of the correlation (deep convective fraction for the Andes). In general, the R^2 for the Amazon and Andes is small in comparison to the western regions, which is probably linked to the high frequency of rain events with a similar composite of rain types. In contrast, the western regions, where shallow convection events clearly differ from highly depleting MCS events, reveal a more robust correlation. The most important change correlating one of the two newly defined fractions with $\delta^{18}\text{O}_p$ reveals a consistent regression sign for each region, so for west and east of the climate divide. Consequently, the dipole pattern that emerges when using the stratiform fraction (Figure 5) disappears. The deep convective fraction is consistently negatively correlated to the $\delta^{18}\text{O}_p$, whereas the shallow convective fraction exhibits a relatively positive sign. Hence, the deep or the shallow convective fraction are insensitive to a prevailing maritime or continental climate. This suggests a more robust and physically based approach representing the relation between $\delta^{18}\text{O}_p$ and rain type.

4 Conclusions

In our modeling approach with the isotope-enabled and convection-permitting COSMO_{iso} model, we documented and analyzed the opposing sign of the correlation between stratiform fraction and $\delta^{18}\text{O}_p$ for west (negative) and east (positive) of the Andean climate divide. The differing strengths of depletion for stratiform, shallow and deep convective rains and their relative contributions to local precipitation are in this respect of particular importance.

Shallow convection and strictly stratiform precipitation yielded the most enriched $\delta^{18}\text{O}_p$, whereas deep convection leads to the most depleted $\delta^{18}\text{O}_p$ followed by mixed rain. Shallow convection is of particular importance for total rain west of the climate divide, whereas deep convection mostly contributes to precipitation east of the climate divide. By definition, a stratiform fraction of 0 % means 100 % convective rain. The latter has usually not been separated

699 into shallow and deep convection in past research. As these two subclasses are associated with
 700 differing $\delta^{18}\text{O}_\text{P}$ signals, the sign of correlation between stratiform fraction and $\delta^{18}\text{O}_\text{P}$ is
 701 determined by the prevailing type of convection within a region and consequently leads to
 702 opposing correlation signs. Therefore, using the stratiform fraction in stable isotope analysis
 703 might lead to ambiguous results. The application of the stratiform fraction has its justification,
 704 since tropical stratiform rain usually occurs together with deep convection like in MCS.
 705 However, we want to underline that it is the deep convection that is responsible for most of the
 706 depletion and not the stratiform rain. Consequently, we suggest, based on our derived $\delta^{18}\text{O}_\text{P}$
 707 dependence on rain type, to use the physically more consistent deep convective fraction or
 708 shallow convective fraction for stable isotope analysis (see Section 3.4). Both metrics take into
 709 account that deep convection leads to most of the depletion, whereas on the other side, shallow
 710 convection and stratiform rain exhibit smaller depletion rates or even enrichment.

711 In summary our main results are

- 712 • Different rain types (stratiform, shallow and deep convective rain) are associated with distinct
 713 $\delta^{18}\text{O}_\text{P}$ and deuterium excess signals
- 714 • Deep convection leads to the strongest $\delta^{18}\text{O}_\text{P}$ depletion rate and the highest d-excess.
- 715 • It is advantageous to utilize a deep convective fraction or shallow convective fraction for
 716 correlations with $\delta^{18}\text{O}_\text{P}$.

717 The study results are limited by the small number of stable isotopic measurements
 718 available for evaluating the model output. Moreover, COSMO_{iso} comprises a one-moment
 719 microphysics scheme that does only account for two ice species (snow and ice, not graupel and
 720 hail). However, it is to be expected that graupel and hail amounts are small in higher order
 721 microphysics schemes, which can be seen for example in the vertical distribution of
 722 hydrometeors in the study of Mölg and Kaser (2011) for a tropical, equatorial high mountain in
 723 Africa.

724 Our results might be of particular interest for, and applicable to paleoclimate studies. The
 725 identification of different rain types could help to interpret seasonally resolved climate proxies
 726 like stable isotopes of tree ring cellulose in Ecuador, with respect to convective activity.
 727 Questions that remain for future studies to be considered are for instance as follows:

- 728 • Do seasonally resolved climate proxies conserve the isotope signature from the occurrence of
 729 different rain types?
- 730 • How does the distribution of rain types change in the course of a year and even longer time
 731 scales?
- 732 • Is the relationship between $\delta^{18}\text{O}_\text{P}$ and deep convective fraction or shallow convective fraction
 733 consistent all over the tropics?

734 To answer these questions in subsequent studies, we plan to extend the model simulations
 735 to multiple years. Moreover, in an upcoming study, we want to compare these model results with
 736 seasonally resolved stable isotope measurements of collected tree ring material.

737 Acknowledgments

738 This study was funded by the Friedrich-Alexander-Universität Erlangen-Nürnberg. The authors gratefully
 739 acknowledge the scientific support and the supply of resources provided by the High Performance Computing

Center (NHR@FAU) of the Friedrich-Alexander-Universität Erlangen-Nürnberg (FAU) under the NHR project b128dc / ATMOS ("Numerical atmospheric modelling for the attribution of climate change and for model improvement"). NHR funding is provided by federal and Bavarian state authorities. NHR@FAU hardware is partially funded by the German Research Foundation (DFG) – 440719683. We acknowledge the provision of the AWS data that benefited from the financial support granted by the German Science Foundation (DFG project code BR1895/29-1) within research unit 2730 RESPECT, Martin Werner for providing the ECHAM6-wiso data; and Hans-Jürgen Panitz for his effort finding a suitable model setup for our study region.

747

748 Open Research

749 The MODIS AQUA and TERRA data can be accessed via http://dx.doi.org/10.5067/MODIS/MYD05_L2.006 and
750 http://dx.doi.org/10.5067/MODIS/MOD05_L2.006, respectively (Gao, 2015). The GNIP dataset can be
751 accessed through <https://www.iaea.org/services/networks/gnip> (IAEA/WMO, 2023). ECHAM6-wiso data
752 has been described in detail in (Cauquoin & Werner, 2021) and can be accessed
753 through <https://doi.org/10.5281/zenodo.5636328> or by contacting one of the authors of this study. All
754 details to the COSMOiso model can found in Pfahl et al. (2012). Processed data and simulation output, the
755 Python code for reproducing the figures and the automatic weather station data can be accessed via
756 <https://doi.org/10.5281/zenodo.10438579> (Landshuter et al., 2023).
757

758

References

- 759 Aemisegger, F., Pfahl, S., Sodemann, H., Lehner, I., Seneviratne, S. I., & Wernli, H. (2014). Deuterium excess as a
760 proxy for continental moisture recycling and plant transpiration. *Atmospheric Chemistry and Physics*,
761 *14*(8), 4029-4054. <https://doi.org/10.5194/acp-14-4029-2014>
- 762 Aemisegger, F., Spiegel, J. K., Pfahl, S., Sodemann, H., Eugster, W., & Wernli, H. (2015). Isotope meteorology of
763 cold front passages: A case study combining observations and modeling. *Geophysical Research Letters*,
764 *42*(13), 5652-5660. <https://doi.org/10.1002/2015gl063988>
- 765 Aggarwal, P. K., Romatschke, U., Araguas-Araguas, L., Belachew, D., Longstaffe, F. J., Berg, P., Schumacher, C.,
766 & Funk, A. (2016). Proportions of convective and stratiform precipitation revealed in water isotope ratios.
767 *Nature Geoscience*, *9*(8), 624-629. <https://doi.org/10.1038/Ngeo2739>
- 768 Allen, R. G., Pereira, L. S., Raes, D., & Smith, R. (1998). *Crop evapotranspiration - Guidelines for computing crop*
769 *water requirements* (Vol. 56). FAO - Food and Agriculture Organization of the United Nations.
- 770 Ampuero, A., Strikis, N. M., Apaéstegui, J., Vuille, M., Novello, V. F., Espinoza, J. C., Cruz, F. W., Vonhof, H.,
771 Mayta, V. C., Martins, V. T. S., Cordeiro, R. C., Azevedo, V., & Sifeddine, A. (2020). The Forest Effects
772 on the Isotopic Composition of Rainfall in the Northwestern Amazon Basin. *Journal of Geophysical*
773 *Research-Atmospheres*, *125*(4). <https://doi.org/10.1029/2019JD031445>
- 774 Asensio, H., Messmer, M., Lüthi, D., Osterried, K., & Jucker, J. (2020). *External Parameters for Numerical*
775 *Weather Prediction and Climate Application EXTPAR. User and Implementation Guide*.
- 776 Baldauf, M., Seifert, A., Forstner, J., Majewski, D., Raschendorfer, M., & Reinhardt, T. (2011). Operational
777 Convective-Scale Numerical Weather Prediction with the COSMO Model: Description and Sensitivities.
778 *Monthly weather review*, *139*(12), 3887-3905. <https://doi.org/10.1175/Mwr-D-10-05013.1>
- 779 Ban, N., Schmidli, J., & Schär, C. (2014). Evaluation of the convection-resolving regional climate modeling
780 approach in decade-long simulations. *Journal of Geophysical Research-Atmospheres*, *119*(13).
781 <https://doi.org/10.1002/2014jd021478>
- 782 Bendix, J., Gaemmerler, S., & Reudenbach, C. (2003). A case study on rainfall dynamics during El Niño/La Niña
783 1997/99 in Ecuador and surrounding areas as inferred from GOES-8 and TRMM-PR observations.
784 *Erdkunde*, *57*(2), 81-93. <https://doi.org/10.3112/erdkunde.2003.02.01>
- 785 Bendix, J., & Lauer, W. (1992). Die Niederschlagsjahreszeiten in Ecuador und ihre klimadynamische Interpretation.
786 *Erdkunde*, *46*, 118-134. <https://doi.org/10.3112/erdkunde.1992.02.04>
- 787 Bendix, J., Trachte, K., Cermak, J., Rollenbeck, R., & Nauss, T. (2009). {Formation of Convective Clouds at the
788 Foothills of the Tropical Eastern Andes (South Ecuador)}. *Journal of Applied Meteorology and*
789 *Climatology*, *48*(8), 1682-1695. <https://doi.org/10.1175/2009jamc2078.1>
- 790 Bony, S., Risi, C., & Vimeux, F. (2008). Influence of convective processes on the isotopic composition (delta O-18
791 and delta D) of precipitation and water vapor in the tropics: 1. Radiative-convective equilibrium and
792 Tropical Ocean-Global Atmosphere-Coupled Ocean-Atmosphere Response Experiment (TOGA-COARE)

- 793 simulations. *Journal of Geophysical Research-Atmospheres*, 113(D19).
 794 <https://doi.org/10.1029/2008jd009942>
- 795 Breil, M., Christner, E., Cauquoin, A., Werner, M., & Schädler, G. (2020). The dependency of the $\delta^{18}\text{O}$ discrepancy
 796 between ice cores and model simulations on the spatial model resolution. *Climate of the Past, Preprint*.
- 797 Campozano, L., Trachte, K., Celleri, R., Samaniego, E., Bendix, J., Albuja, C., & Mejia, J. F. (2018). Climatology
 798 and Teleconnections of Mesoscale Convective Systems in an Andean Basin in Southern Ecuador: The Case
 799 of the Paute Basin. *Advances in Meteorology*. <https://doi.org/10.1155/2018/4259191>
- 800 Capotondi, A., Wittenberg, A., Newman, M., Lorenzo, E. D., Yu, J. Y., Braconnot, P., Cole, J., Dewitte, B., Giese,
 801 B., Guilyardi, E., Jin, F. F., Karnauskas, K. B., Kirtman, B., Lee, T., Schneider, N., Xue, Y., & Yeh, S. W.
 802 (2015). Understanding ENSO diversity. *Bulletin of the American Meteorological Society*, 96(6), 921-938.
 803 <https://doi.org/10.1175/BAMS-D-13-00117.1>
- 804 Cauquoin, A., & Werner, M. (2021). High-Resolution Nudged Isotope Modeling With ECHAM6-Wiso: Impacts of
 805 Updated Model Physics and ERA5 Reanalysis Data. *Journal of Advances in Modeling Earth Systems*,
 806 13(11). <https://doi.org/10.1029/2021MS002532>
- 807 Chimborazo, O., & Vuille, M. (2021). Present-day climate and projected future temperature and precipitation
 808 changes in Ecuador. *Theoretical and Applied Climatology*, 143(3-4), 1581-1597.
 809 <https://doi.org/10.1007/s00704-020-03483-y>
- 810 Christner, E., Aemisegger, F., Pfahl, S., Werner, M., Cauquoin, A., Schneider, M., Hase, F., Barthlott, S., &
 811 Schädler, G. (2018). The Climatological Impacts of Continental Surface Evaporation, Rainout, and
 812 Subcloud Processes on D of Water Vapor and Precipitation in Europe. *Journal of Geophysical Research-*
 813 *Atmospheres*, 123(8), 4390-4409. <https://doi.org/10.1002/2017jd027260>
- 814 Ciais, P., & Jouzel, J. (1994). Deuterium and Oxygen-18 in Precipitation - Isotopic Model, Including Mixed Cloud
 815 Processes. *Journal of Geophysical Research-Atmospheres*, 99(D8), 16793-16803.
 816 <https://doi.org/10.1029/94jd00412>
- 817 Collier, E., Sauter, T., Mölg, T., & Hardy, D. (2019). The Influence of Tropical Cyclones on Circulation, Moisture
 818 Transport, and Snow Accumulation at Kilimanjaro During the 2006-2007 Season. *Journal of Geophysical*
 819 *Research-Atmospheres*, 124(13), 6919-6928. <https://doi.org/10.1029/2019jd030682>
- 820 Dansgaard, W. (1964). Stable isotopes in precipitation. *Tellus*, 16, 436-468.
 821 <https://doi.org/10.3402/tellusa.v16i4.8993>
- 822 de Vries, A. J., Aemisegger, F., Pfahl, S., & Wernli, H. (2022). Stable water isotope signals in tropical ice clouds in
 823 the West African monsoon simulated with a regional convection-permitting model. *Atmospheric Chemistry*
 824 *and Physics*, 22(13), 8863-8895. <https://doi.org/10.5194/acp-22-8863-2022>
- 825 Dee, S., Bailey, A., Conroy, J. L., Atwood, A., Stevenson, S., Nusbaumer, J., & Noone, D. (2023). Water isotopes,
 826 climate variability, and the hydrological cycle: recent advances and new frontiers. *Environmental*
 827 *Research: Climate*, 2 (022002). <https://doi.org/10.1088/2752-5295/accbe1>
- 828 Doms, G., Förstner, J., Heise, E., Herzog, H.-J., Mironov, D., Raschendorfer, M., Reinhardt, T., Ritter, B., Schrodin,
 829 R., Schulz, J.-P., & Vogel, G. (2011). *A Description of the Nonhydrostatic Regional COSMO Model. Part*
 830 *II: Physical Parameterization*. Deutscher Wetterdienst.
- 831 Emck, P. (2008). *A Climatology of South Ecuador: With Special Focus on the Major Andean Climate Divide*. VDM
 832 Verlag.
- 833 Feng, Z., Leung, L. R., Liu, N. N., Wang, J. Y., Houze, R. A., Li, J. F., Hardin, J. C., Chen, D. D., & Guo, J. P.
 834 (2021). A Global High-Resolution Mesoscale Convective System Database Using Satellite-Derived Cloud
 835 Tops, Surface Precipitation, and Tracking. *Journal of Geophysical Research-Atmospheres*, 126(8).
 836 [https://doi.org/ARTN](https://doi.org/ARTN%2020JD034202) e2020JD034202
 837 10.1029/2020JD034202
- 838 Fosser, G., Khodayar, S., & Berg, P. (2015). Benefit of convection permitting climate model simulations in the
 839 representation of convective precipitation. *Climate Dynamics*, 44(1-2), 45-60.
 840 <https://doi.org/10.1007/s00382-014-2242-1>
- 841 Fröhlich, K., Gibson, J., & Aggarwal, P. K. (2002). *Deuterium excess in precipitation and its climatological*
 842 *significance* Proceedings of the study of environmental change using isotope techniques, Vienna (Austria).
- 843 Fröhlich, K., Kralik, M., Papesch, W., Rank, D., Scheffinger, H., & Stichler, W. (2008). Deuterium excess in
 844 precipitation of Alpine regions - moisture recycling. *Isotopes in Environmental and Health Studies*, 44(1),
 845 61-70. <https://doi.org/10.1080/10256010801887208>
- 846 Funk, A., Schumacher, C., & Awaka, J. (2013). Analysis of Rain Classifications over the Tropics by Version 7 of
 847 the TRMM PR 2A23 Algorithm. *Journal of the Meteorological Society of Japan*, 91(3), 257-272.
 848 <https://doi.org/10.2151/jmsj.2013-302>

- 849 Gao, B. (2015). *MODIS Atmosphere L2 Water Vapor Product*. NASA MODIS Adaptive Processing System, Goddard
 850 Space Flight Center https://doi.org/10.5067/MODIS/MOD05_L2.006
- 851 Gao, J., Masson-Delmotte, V., Risi, C., He, Y., & Yao, T. (2013). What controls precipitation delta O-18 in the
 852 southern Tibetan Plateau at seasonal and intra-seasonal scales? A case study at Lhasa and Nyalam. *Tellus*
 853 *Series B-Chemical and Physical Meteorology*, 65. <https://doi.org/10.3402/tellusb.v65i0.21043>
- 854 Garcia, M., Villalba, F., Araguas-Araguas, L., & Rozanski, K. (1998). The role of atmospheric circulation patterns
 855 in controlling the regional distribution of stable isotope contents in precipitation: Preliminary results from
 856 two transects in the Ecuadorian Andes. In *Isotope Techniques in the Study of Environmental Change* (pp.
 857 127-140). International Atomic Energy Agency.
- 858 Gat, J. R. (1996). Oxygen and hydrogen isotopes in the hydrologic cycle. *Annual Review of Earth and Planetary*
 859 *Sciences*, 24, 225-262. <https://doi.org/10.1146/annurev.earth.24.1.225>
- 860 Gonfiantini, R., Roche, M. A., Olivry, J. C., Fontes, J. C., & Zuppi, G. M. (2001). The altitude effect on the isotopic
 861 composition of tropical rains. *Chemical Geology*, 181(1-4), 147-167. [https://doi.org/10.1016/S0009-2541\(01\)00279-0](https://doi.org/10.1016/S0009-2541(01)00279-0)
- 862 Graf, P., Wernli, H., Pfahl, S., & Sodemann, H. (2019). A new interpretative framework for below-cloud effects on
 864 stable water isotopes in vapour and rain. *Atmospheric Chemistry and Physics*, 19(2), 747-765.
 865 <https://doi.org/10.5194/acp-19-747-2019>
- 866 Hoffmann, G., Ramirez, E., Taupin, J. D., Francou, B., Ribstein, P., Delmas, R., Durr, H., Gallaire, R., Simoes, J.,
 867 Schotterer, U., Stievenard, M., & Werner, M. (2003). Coherent isotope history of Andean ice cores over the
 868 last century. *Geophysical Research Letters*, 30(4). <https://doi.org/10.1029/2002gl014870>
- 869 Houze, R. A. (2004). Mesoscale convective systems. *Reviews of Geophysics*, 42(4).
 870 <https://doi.org/10.1029/2004rg000150>
- 871 Houze, R. A. (2014). *Cloud Dynamics* (2nd ed., Vol. International Geophysics). Elsevier.
- 872 Houze, R. A., Rasmussen, K. L., Zuluaga, M. D., & Brodzik, S. R. (2015). The variable nature of convection in the
 873 tropics and subtropics: A legacy of 16years of the Tropical Rainfall Measuring Mission satellite. *Reviews of*
 874 *Geophysics*, 53(3), 994-1021. <https://doi.org/10.1002/2015rg000488>
- 875 Hu, J., Emile-Geay, J., Nusbaumer, J., & Noone, D. (2018). Impact of Convective Activity on Precipitation delta O-
 876 18 in Isotope-Enabled General Circulation Models. *Journal of Geophysical Research-Atmospheres*,
 877 123(23), 13595-13610. <https://doi.org/10.1029/2018jd029187>
- 878 IAEA/WMO. (2023). *Global Network of Isotopes in Precipitation (GNIP)*
 879 <https://www.iaea.org/services/networks/gnip>
- 880 Johnson, R. H., Rickenbach, T. M., Rutledge, S. A., Ciesielski, P. E., & Schubert, W. H. (1999). Trimodal
 881 characteristics of tropical convection. *Journal of Climate*, 12(8), 2397-2418. [https://doi.org/10.1175/1520-0442\(1999\)012%3C2397:TCOTC%3E2.0.CO;2](https://doi.org/10.1175/1520-0442(1999)012%3C2397:TCOTC%3E2.0.CO;2)
- 882 Klingaman, N. P., Martin, G. M., & Moise, A. (2017). ASoP (v1.0): a set of methods for analyzing scales of
 883 precipitation in general circulation models. *Geoscientific Model Development*, 10(1), 57-83.
 884 <https://doi.org/10.5194/gmd-10-57-2017>
- 885 Korolev, A., McFarquhar, G., Field, P. R., Franklin, C., Lawson, P., Wang, Z., Williams, E., Abel, S. J., Axisa, D.,
 886 Borrmann, S., Crosier, J., Fugal, J., Krämer, M., Lohmann, U., Schlenker, O., Schnaiter, M., & Wendisch,
 887 M. (2017). Mixed-Phase Clouds: Progress and Challenges. *Meteorological Monographs*, 58, 5.1-5.50.
 888 <https://doi.org/10.1175/AMSMONOGRAPHS-D-17-0001.1>
- 889 Kropač, E., Mölg, T., Cullen, N. J., Collier, E., Pickler, C., & Turton, J. V. (2021). A Detailed, Multi-Scale
 890 Assessment of an Atmospheric River Event and Its Impact on Extreme Glacier Melt in the Southern Alps
 891 of New Zealand. *Journal of Geophysical Research-Atmospheres*, 126(9).
 892 <https://doi.org/10.1029/2020JD034217>
- 893 Kurita, N. (2013). Water isotopic variability in response to mesoscale convective system over the tropical ocean.
 894 *Journal of Geophysical Research-Atmospheres*, 118(18), 10376-10390. <https://doi.org/10.1002/jgrd.50754>
- 895 Kurita, N., Noone, D., Risi, C., Schmidt, G. A., Yamada, H., & Yoneyama, K. (2011). Intraseasonal isotopic
 896 variation associated with the Madden-Julian Oscillation. *Journal of Geophysical Research-Atmospheres*,
 897 116. <https://doi.org/10.1029/2010jd015209>
- 898 Lacour, J. L., Risi, C., Worden, J., Clerbaux, C., & Coheur, P. F. (2018). Importance of depth and intensity of
 899 convection on the isotopic composition of water vapor as seen from IASI and TES delta D observations.
 900 *Earth and Planetary Science Letters*, 481, 387-394. <https://doi.org/10.1016/j.epsl.2017.10.048>
- 901 Landshuter, N., Aemisegger, F., & Mölg, T. (2023). *Data and Code: Stable water isotope signals and their relation*
 902 *to stratiform and convective precipitation in the tropical Andes*. Zenodo.
 903 <https://doi.org/10.5281/zenodo.10438579>
- 904

- 905 Landshuter, N., Mölg, T., Griebinger, J., Bräuning, A., & Peters, T. (2020). 10-year Characteristics of Moisture
 906 Source Regions and Their Potential Effect on Seasonal Isotopic Signatures of delta O-18 in Tropical Trees
 907 of Southern Ecuador. *Frontiers in Earth Science*, 8. <https://doi.org/10.3389/feart.2020.604804>
- 908 Lee, J. E., & Fung, I. (2008). "Amount effect" of water isotopes and quantitative analysis of post-condensation
 909 processes. *Hydrological Processes*, 22(1), 1-8. <https://doi.org/10.1002/hyp.6637>
- 910 Lee, K. O., Aemisegger, F., Pfahl, S., Flamant, C., Lacour, J. L., & Chaboureaud, J. P. (2019). Contrasting stable
 911 water isotope signals from convective and large-scale precipitation phases of a heavy precipitation event in
 912 southern Italy during HyMeX IOP 13: a modelling perspective. *Atmospheric Chemistry and Physics*,
 913 19(11), 7487-7506. <https://doi.org/10.5194/acp-19-7487-2019>
- 914 Lekshmy, P. R., Midhun, M., Ramesh, R., & Jani, R. A. (2014). O-18 depletion in monsoon rain relates to large
 915 scale organized convection rather than the amount of rainfall. *Scientific Reports*, 4.
 916 <https://doi.org/10.1038/srep05661>
- 917 Liu, X. D., Osher, S., & Chan, T. (1994). Weighted Essentially Nonoscillatory Schemes. *Journal of Computational*
 918 *Physics*, 115(1), 200-212. <https://doi.org/10.1006/jcph.1994.1187>
- 919 Marshall, J., & Plumb, R. A. (2008). *Atmosphere, Ocean and Climate Dynamics. An Introductory Text.* (R.
 920 Dmowska, D. Hartmann, & T. Rossby, Eds. Vol. 93). Elsevier.
- 921 McCarroll, D., & Loader, N. J. (2004). Stable isotopes in tree rings. *Quaternary Science Reviews*, 23(7-8), 771-801.
 922 <https://doi.org/10.1016/j.quascirev.2003.06.017>
- 923 McPhaden, M. J., Zebiak, S. E., & Glantz, M. H. (2006). ENSO as an integrating concept in Earth science. *Science*,
 924 314(5806), 1740-1745. <https://doi.org/10.1126/science.1132588>
- 925 Mellor, G. L., & Yamada, T. (1974). Hierarchy of Turbulence Closure Models for Planetary Boundary-Layers.
 926 *Journal of the Atmospheric Sciences*, 31(7), 1791-1806. [https://doi.org/10.1175/1520-0469\(1974\)031%3C1791:AHOTCM%3E2.0.CO;2](https://doi.org/10.1175/1520-0469(1974)031%3C1791:AHOTCM%3E2.0.CO;2)
- 927
 928 Merlivat, L., & Jouzel, J. (1979). Global Climatic Interpretation of the Deuterium-Oxygen-18 Relationship for
 929 Precipitation. *Journal of Geophysical Research-Oceans*, 84(Nc8), 5029-5033.
 930 <https://doi.org/10.1029/JC084iC08p05029>
- 931 Mölders, N., & Kramm, G. (2014). *Lectures in Meteorology.* Springer. <https://doi.org/10.1007/978-3-319-02144-7>
- 932 Mölg, T., Grosshauser, M., Hemp, A., Hofer, M., & Marzeion, B. (2012). Limited forcing of glacier loss through
 933 land-cover change on Kilimanjaro. *Nature Climate Change*, 2(4), 254-258.
 934 <https://doi.org/10.1038/Nclimate1390>
- 935 Mölg, T., & Kaser, G. (2011). A new approach to resolving climate-cryosphere relations: Downscaling climate
 936 dynamics to glacier-scale mass and energy balance without statistical scale linking. *Journal of Geophysical*
 937 *Research-Atmospheres*, 116. <https://doi.org/10.1029/2011jd015669>
- 938 Moore, M., Kuang, Z., & Blossey, P. N. (2014). A moisture budget perspective of the amount effect. *Geophysical*
 939 *Research Letters*, 41(4), 1329-1335. <https://doi.org/10.1002/2013gl058302>
- 940 Munksgaard, N. C., Kurita, N., Sanchez-Murillo, R., Ahmed, N., Araguas, L., Balachew, D. L., Bird, M. I.,
 941 Chakraborty, S., Chinh, N. K., Cobb, K. M., Ellis, S. A., Esquivel-Hernandez, G., Ganyaglo, S. Y., Gao, J.,
 942 Gastmans, D., Kaseke, K. F., Kebede, S., Morales, M. R., Mueller, M., . . . Zwart, C. (2019). Data
 943 Descriptor: Daily observations of stable isotope ratios of rainfall in the tropics. *Scientific Reports*, 9.
 944 <https://doi.org/10.1038/s41598-019-50973-9>
- 945 Natali, S., Doveri, M., Gianecchini, R., Baneschi, I., & Zanchetta, G. (2022). Is the deuterium excess in
 946 precipitation a reliable tracer of moisture sources and water resources fate in the western Mediterranean?
 947 New insights from Apuan Alps (Italy). *Journal of Hydrology*, 614.
 948 <https://doi.org/10.1016/j.jhydrol.2022.128497>
- 949 Panitz, H. J., Dosio, A., Buchner, M., Luthi, D., & Keuler, K. (2014). COSMO-CLM (CCLM) climate simulations
 950 over CORDEX-Africa domain: analysis of the ERA-Interim driven simulations at 0.44A degrees and 0.22A
 951 degrees resolution. *Climate Dynamics*, 42(11-12), 3015-3038. <https://doi.org/10.1007/s00382-013-1834-5>
- 952 Pfahl, S., & Sodemann, H. (2014). What controls deuterium excess in global precipitation? *Climate of the Past*, 10,
 953 771-781. <https://doi.org/10.5194/cp-10-771-2014>
- 954 Pfahl, S., Wernli, H., & Yoshimura, K. (2012). The isotopic composition of precipitation from a winter storm - a
 955 case study with the limited-area model COSMOiso. *Atmospheric Chemistry and Physics*, 12(3), 1629-1648.
 956 <https://doi.org/10.5194/acp-12-1629-2012>
- 957 Prein, A. F., Ge, M., Valle, A. R., Wang, D., & Giangrande, S. E. (2022). Towards a Unified Setup to Simulate Mid-
 958 Latitude and Tropical Mesoscale Convective Systems at Kilometer-Scales. *Earth and Space Science*, 9(8).
 959 <https://doi.org/10.1029/2022EA002295>

- 960 Pucha-Cofrep, D., Peters, T., & Bräuning, A. (2015). Wet season precipitation during the past century reconstructed
 961 from tree-rings of a tropical dry forest in Southern Ecuador. *Global and Planetary Change*, 133, 65-78.
 962 <https://doi.org/10.1016/j.gloplacha.2015.08.003>
- 963 Risi, C., Bony, S., & Vimeux, F. (2008). Influence of convective processes on the isotopic composition (δ O-18
 964 and δ D) of precipitation and water vapor in the tropics: 2. Physical interpretation of the amount effect.
 965 *Journal of Geophysical Research-Atmospheres*, 113(D19). <https://doi.org/10.1029/2008jd009943>
- 966 Risi, C., Muller, C., & Blossey, P. (2020). What Controls the Water Vapor Isotopic Composition Near the Surface of
 967 Tropical Oceans? Results From an Analytical Model Constrained by Large-Eddy Simulations. *Journal of*
 968 *Advances in Modeling Earth Systems*, 12(8). <https://doi.org/10.1029/2020MS002106>
- 969 Ritter, B., & Geleyn, J. F. (1992). A Comprehensive Radiation Scheme for Numerical Weather Prediction Models
 970 with Potential Applications in Climate Simulations. *Monthly weather review*, 120(2), 303-325.
 971 [https://doi.org/10.1175/1520-0493\(1992\)120%3C0303:ACRSFN%3E2.0.CO;2](https://doi.org/10.1175/1520-0493(1992)120%3C0303:ACRSFN%3E2.0.CO;2)
- 972 Rollenbeck, R., & Bendix, J. (2011). Rainfall distribution in the Andes of southern Ecuador derived from blending
 973 weather radar data and meteorological field observations. *Atmospheric Research*, 99(2), 277-289.
 974 <https://doi.org/10.1016/j.atmosres.2010.10.018>
- 975 Samuels-Crow, K. E., Galewsky, J., Sharp, Z. D., & Dennis, K. J. (2014). Deuterium excess in subtropical free
 976 troposphere water vapor: Continuous measurements from the Chajnantor Plateau, northern Chile.
 977 *Geophysical Research Letters*, 41(23), 8652-8659. <https://doi.org/10.1002/2014GL062302>
- 978 Schättler, U., Doms, G., & Schraff, C. (2013). *A Description of the Nonhydrostatic Regional COSMO-Model. Part*
 979 *VII. User's Guide* (U. Schättler, Ed.). Deutscher Wetterdienst Business Area "Research and Development".
- 980 Schumacher, C., & Houze, R. A. (2003). Stratiform rain in the tropics as seen by the TRMM precipitation radar.
 981 *Journal of Climate*, 16(11), 1739-1756. [https://doi.org/10.1175/1520-0442\(2003\)016%3C1739:SRITTA%3E2.0.CO;2](https://doi.org/10.1175/1520-0442(2003)016%3C1739:SRITTA%3E2.0.CO;2)
- 982 Spannll, S., Volland, F., Pucha, D., Peters, T., Cueva, E., & Bräuning, A. (2016). Climate variability, tree increment
 983 patterns and ENSO-related carbon sequestration reduction of the tropical dry forest species *Loxopterygium*
 984 *huasango* of Southern Ecuador. *Trees-Structure and Function*, 30(4), 1245-1258.
 985 <https://doi.org/10.1007/s00468-016-1362-0>
- 986 Steppeler, J., Doms, G., Schättler, U., Bitzer, H. W., Gassmann, A., Damrath, U., & Gregoric, G. (2003). Meso-
 987 gamma scale forecasts using the nonhydrostatic model LM. *Meteorology and Atmospheric Physics*, 82(1-
 988 4), 75-96. <https://doi.org/10.1007/s00703-001-0592-9>
- 989 Su, J. Z., Xiang, B. Q., Wang, B., & Li, T. (2014). Abrupt termination of the 2012 Pacific warming and its
 990 implication on ENSO prediction. *Geophysical Research Letters*, 41(24), 9058-9064.
 991 <https://doi.org/10.1002/2014gl062380>
- 992 Sui, C. H., Tsay, C. T., & Li, X. F. (2007). Convective - stratiform rainfall separation by cloud content. *Journal of*
 993 *Geophysical Research-Atmospheres*, 112(D14). <https://doi.org/10.1029/2006jd008082>
- 994 Temme, F., Turton, J. V., Mölg, T., & Sauter, T. (2020). Flow Regimes and Fohn Types Characterize the Local
 995 Climate of Southern Patagonia. *Atmosphere*, 11(9). <https://doi.org/10.3390/atmos11090899>
- 996 Tharammal, T., Bala, G., & Noone, D. (2017). Impact of deep convection on the isotopic amount effect in tropical
 997 precipitation. *Journal of Geophysical Research-Atmospheres*, 122(3), 1505-1523.
 998 <https://doi.org/10.1002/2016jd025555>
- 999 Thompson, L. G., Mosley-Thompson, E., & Henderson, K. A. (2000). Ice-core palaeoclimate records in tropical
 1000 South America since the Last Glacial Maximum. *Journal of Quaternary Science*, 15(4), 377-394.
 1001 [https://doi.org/10.1002/1099-1417\(200005\)15:4%3C377::AID-JQS542%3E3.0.CO;2-L](https://doi.org/10.1002/1099-1417(200005)15:4%3C377::AID-JQS542%3E3.0.CO;2-L)
- 1002 Thurnherr, I., Hartmuth, K., Jansing, L., Gehring, J., Boettcher, M., Gorodetskaya, I., Werner, M., Wernli, H., &
 1003 Aemisegger, F. (2021). The role of air-sea fluxes for the water vapour isotope signals in the cold and warm
 1004 sectors of extratropical cyclones over the Southern Ocean. *Weather Clim. Dynam.*, 2(2), 331-357.
 1005 <https://doi.org/10.5194/wcd-2-331-2021>
- 1006 Tiedtke, M. (1989). A Comprehensive Mass Flux Scheme for Cumulus Parameterization in Large-Scale Models.
 1007 *Monthly weather review*, 117(8), 1779-1800. [https://doi.org/10.1175/1520-0493\(1989\)117%3C1779:ACMFSF%3E2.0.CO;2](https://doi.org/10.1175/1520-0493(1989)117%3C1779:ACMFSF%3E2.0.CO;2)
- 1008 Trachte, K. (2018). Atmospheric Moisture Pathways to the Highlands of the Tropical Andes: Analyzing the Effects
 1009 of Spectral Nudging on Different Driving Fields for Regional Climate Modeling. *Atmosphere*, 9(11).
 1010 <https://doi.org/10.3390/atmos9110456>
- 1011 Vargas, D., Chimborazo, O., Laszlo, E., Temovski, M., & Palcsu, L. (2022). Rainwater Isotopic Composition in the
 1012 Ecuadorian Andes and Amazon Reflects Cross-Equatorial Flow Seasonality. *Water*, 14(13).
 1013 <https://doi.org/10.3390/w14132121>
- 1014
 1015

- 1016 Vergara-Temprado, J., Ban, N., Panosetti, D., Schlemmer, L., & Schar, C. (2020). Climate Models Permit
1017 Convection at Much Coarser Resolutions Than Previously Considered. *Journal of Climate*, 33(5), 1915-
1018 1933. <https://doi.org/10.1175/Jcli-D-19-0286.1>
- 1019 Victoria, R. L., Martinelli, L. A., Mortatti, J., & Richey, J. (1991). Mechanisms of Water Recycling in the Amazon
1020 Basin - Isotopic Insights. *Ambio*, 20(8), 384-387. (<https://www.jstor.org/stable/4313869>)
- 1021 Villiger, L., Dütsch, M., Bony, S., Lothon, M., Pfahl, S., Wernli, H., Brilouet, P.-E., Chazette, P., Coutris, P.,
1022 Delanoë, J., Flamant, C., Schwarzenboeck, A., Werner, M., & Aemisegger, F. (2023). Water isotopic
1023 characterisation of the cloud-circulation coupling in the North Atlantic trades. Part 1: A process-oriented
1024 evaluation of COSMOiso simulations with EUREC4A observations. *EGUsphere [preprint]*.
1025 <https://doi.org/10.5194/egusphere-2023-449>
- 1026 Vimeux, F., Gallaire, R., Bony, S., Hoffmann, G., & Chiang, J. C. H. (2005). What are the climate controls on delta
1027 D in precipitation in the Zongo Valley (Bolivia)? Implications for the Illimani ice core interpretation. *Earth
1028 and Planetary Science Letters*, 240(2), 205-220. <https://doi.org/10.1016/j.epsl.2005.09.031>
- 1029 Volland-Voigt, F., Bräuning, A., Ganzhi, O., Peters, T., & Maza, H. (2011). Radial stem variations of *Tabebuia
1030 chrysantha* (Bignoniaceae) in different tropical forest ecosystems of southern Ecuador. *Trees-Structure and
1031 Function*, 25(1), 39-48. <https://doi.org/10.1007/s00468-010-0461-6>
- 1032 Wang, B. (1994). Climatic Regimes of Tropical Convection and Rainfall. *Journal of Climate*, 7(7), 1109-1118.
1033 [https://doi.org/10.1175/1520-0442\(1994\)007%3C1109:CROTCA%3E2.0.CO;2](https://doi.org/10.1175/1520-0442(1994)007%3C1109:CROTCA%3E2.0.CO;2)
- 1034 Wang, B., & Xu, X. H. (1997). Northern hemisphere summer monsoon singularities and climatological intraseasonal
1035 oscillation. *Journal of Climate*, 10(5), 1071-1085. [https://doi.org/10.1175/1520-
1036 0442\(1997\)010%3C1071:NHMSA%3E2.0.CO;2](https://doi.org/10.1175/1520-0442(1997)010%3C1071:NHMSA%3E2.0.CO;2)
- 1037 Wilks, D. S. (2011). *Statistical Methods in the Atmospheric Sciences* (R. Dmowska, D. Hartmann, & H. T. Rossby,
1038 Eds. Vol. 100). Academic Press.
- 1039 Zhiña, D. X., Mosquera, G. M., Esquivel-Hernández, G., Córdova, M., Sánchez-Murillo, R., Orellana-Alvear, J., &
1040 Crespo, P. (2022). Hydrometeorological Factors Controlling the Stable Isotopic Composition of
1041 Precipitation in the Highlands of South Ecuador. *Journal of Hydrometeorology*, 23(7), 1059-1074.
1042 <https://doi.org/10.1175/Jhm-D-21-0180.1>
- 1043 Zwart, C., Munksgaard, N. C., Kurita, N., & Bird, M. I. (2016). Stable isotopic signature of Australian monsoon
1044 controlled by regional convection. *Quaternary Science Reviews*, 151, 228-235.
1045 <https://doi.org/10.1016/j.quascirev.2016.09.010>
1046